Journal of Nuclear Materials 383 (2008) 153–171

Contents lists available at ScienceDirect

Journal of Nuclear Materials

journal homepage: www.elsevier.com/locate/jnucmat

Microstructural evolution in zirconium based alloys

R. Tewari [a], D. Srivastava [a,*], G.K. Dey [a], J.K. Chakravarty [b], S. Banerjee [c,1]

[a] Materials Science Division, Bhabha Atomic Research Centre, Mumbai 400 085, India
[b] Mechanical Metallurgy Section, Bhabha Atomic Research Centre, Mumbai 400 085, India
[c] Bhabha Atomic Research Centre, Mumbai 400 085, India

A B S T R A C T

Zirconium alloys which exhibit practically all possible solid state phase transformations offer some unique opportunities for studying the fundamental aspects of phase transformations. The crystallographic features associated with the phase changes are much simpler in zirconium based systems, making them more suitable for providing a basic understanding of the relevant phenomena. Some of the important issues related to phase transformations research are identified and the manner, in which studies in zirconium alloys have contributed to the understanding of these issues, is discussed in this paper. Both the types of displacive transformations – shear-dominated and shuffle dominated – are encountered in zirconium alloys. The crystallography and the mechanism of such transformations are discussed, giving special reference to the morphological and sub-structural changes in zirconium martensites and to the fine particle and plate-shaped morphologies of the ω-phase. Morphological and crystallographical features of displacive and diffusional transformations have been compared. Several examples of mixed mode transformations, viz., the formation of γ-hydride phase, the active eutectoid decomposition and the formation of ordered ω-phases are cited and their respective mechanisms described.

1. Introduction

Zirconium based alloy components form the major part of the in-core structural material in heavy water and water cooled nuclear reactors. The performance of these components is very critical for a safe and economically viable operation of the reactors. Depending on the service requirements, zirconium alloy components used in nuclear reactors are processed in different manner to achieve the best combination of properties. Microstructural control of these alloys through proper selection of the processing parameters is, therefore, a major challenge posed to metallurgists. In service changes that occur in microstructure determine the service life of these components. This aspect also draws considerable attention.

Microstructures of zirconium based alloys can be tailored to obtain suitable properties in the material by selecting suitable thermo-mechanical processing conditions such as stain rates and temperature. During fabrication of the structural components for nuclear reactors, which involves a complex thermo-mechanical processing, the microstructure developed determine the long and short terms properties of these components [1–3]. In addition, these alloys have shown variety of phase transformations [4–6]. Due to amenability to these phase transformations-involving both difussionless and diffusional transformation – a variety of microstructures can be produced. Evolution of the microstructures, therefore, can be broadly classified in the following categories.

1.1. Evolution of the microstructure by heat treatments

These can further be divided into two categories; microstructural development due to (i) phase transformations occurring upon quenching from the high temperature β-phase field and (ii) phase transformations occurring upon aging subsequent to quenching from the β-phase field. Phase transformation pertaining to the former category are, generally, diffusionless transformations, like martensite, ω-phase transformation etc., or the transformations which can not be suppressed by quenching due to their fast kinetics, for example, active eutectoids observed in the Zr-based alloy systems [7,8]. These transformations are functions of the concentration of solute atoms, the degree of supercooling and the rate of quenching. Transformations pertaining to latter category are mainly diffusional in nature which includes tempering of martensite, isothermal ω formation and precipitation reactions.

1.2. By ingress of hydrogen

Effects of ingress of hydrogen in Zr-based alloys is so pronounced that the life time of Zr alloys inside reactors is

* Corresponding author.
E-mail address: dsrivastavabarc@yahoo.co.in (D. Srivastava).
[1] Director.

0022-3115/$ - see front matter © 2008 Elsevier B.V. All rights reserved.
doi:10.1016/j.jnucmat.2008.08.041

limited by this factor [9]. It is essentially due to the low solubility of hydrogen in the α(hcp) phase which led to the precipitation of hydrides effecting the mechanical properties of the Zr alloys adversely. Moreover, the concentration of the hydrogen atoms increases in the structural components during operation and the diffusion of the hydrogen atoms is so fast in comparison to the solvent atoms that the diffusion of solvent atoms can be considered negligible for all practical purposes. Therefore, hydride formation, exhibits many characteristics of a mixed mode – diffusional + displacive transformation – akin to the 'Bainitic transformation'.

1.3. By hot working

Zirconium based alloys are processed in the α + β-phase field during hot working. During fabrication zirconium alloys exhibit strong tendency for texture [10,11]. Hot working has major influence in the development of texture which influences the properties and life time of components of these alloys in service. Microstructural changes that occur during hot working are primarily governed by the strain and temperature. Dynamic recrystallization and recovery processes are the dominating mechanisms which bring about microstructural changes [12–15]. In addition, precipitation of the intermetallic phases has been noticed in several cases.

1.4. Exposure to pressure

Zr and its alloys exhibit various phase transformations under high pressure conditions [16–19]. Under static conditions transformation sequence $\alpha \rightarrow \omega \rightarrow \beta$ has been observed which is very similar to the sequence observed in Zr alloys upon increasing concentration of the β stabilizers. Under shock pressure conditions, formation of the ω-phase is observed in pure zirconium as well as in β-stabilized alloys.

Many of these microstructural evolution processes can be explained taking example of the Zr–Nb system (phase diagram) with superimposed metastable phase boundaries shown in Fig. 1 which shows the different component composition corresponding to the $\beta \rightarrow \alpha$ and $\beta \rightarrow \omega$, structural instabilities and the β-phase separation. The manifestation of these tendencies also get reflected in the monotectoid $\beta_1 \rightarrow \alpha + \beta_2$ reaction in the phase diagram.

The present paper describes the evolution of microstructures under various conditions. The underlying mechanisms of the formation of different phases are discussed. Some of the issues of general interest to the solid–solid phase transformation mechanisms have been addressed. The roles of lattice correspondences, lattice site correspondences and self accommodation in various transformations in the formation of different product morphologies have been discussed.

2. Displacive transformations

Pure Zr and its dilute alloys with β stabilizing elements transform through several diffusionless transformations when quenched from the β-phase field provided the cooling rate exceeds a certain critical value. As the start temperature of these transformations is a strong function of the solute content, the high temperature β-phase can be stabilized to room temperature increasing concentration of β-stabilizers. These transformations are briefly discussed in the followings.

2.1. Martensitic phase transformation

In Zr base alloys martensites exhibit several morphologies which can be broadly classified into the lath and the plate types (Fig. 2). In case of iodide pure Zr (solute concentration typically lower than 200 ppm) formation of massive martensite has been noticed (Fig. 2(a) and (b)). In the lath type morphology, martensite units are grouped together in parallel arrays within a packet and several such packets make up the volume of the parent β-grain (Fig. 2(c)–(f)). Two types of orientation distributions of laths in a given packet have been reported. In one case, laths belonging to the same orientation variant are stacked together with a small angle boundary separating the adjacent laths while in the other alternate laths are twin related (Fig. 2(c) and (d)). TEM investigations have clearly revealed that a group of laths with the same orientation variant have the small angle tilt boundaries between the adjacent laths with misorientation between the adjacent laths of the order of 1.0–1.5°. Contrast analysis of dislocations constituting these lath boundaries has shown that these dislocations have $\langle c + a \rangle$ type Burgers vectors (Fig. 2(h)) [20]. The alloys which

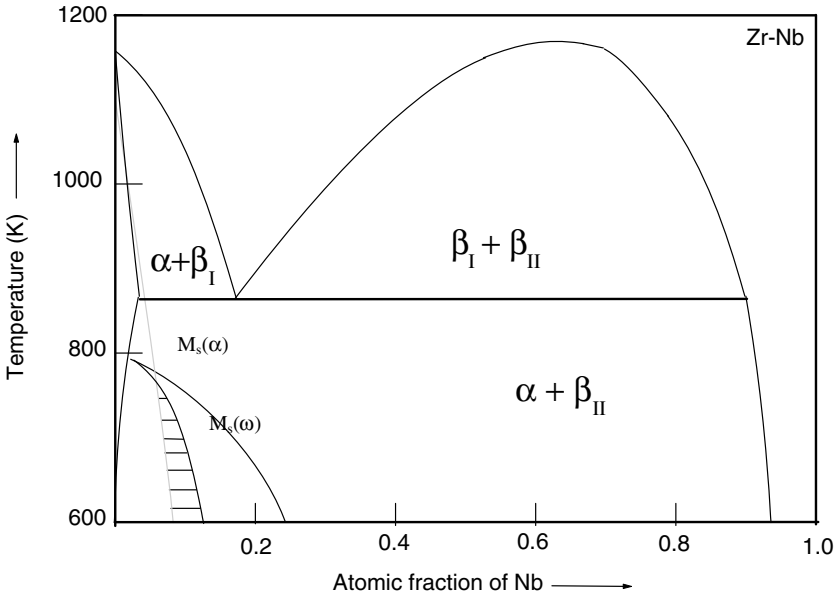

Fig. 1. Phase diagram of the binary Zr–Nb system. The start temperatures of the metastable phases have been superimposed on the phase diagram. The shaded region shows the composition range over which formation of the athermal ω occurs.

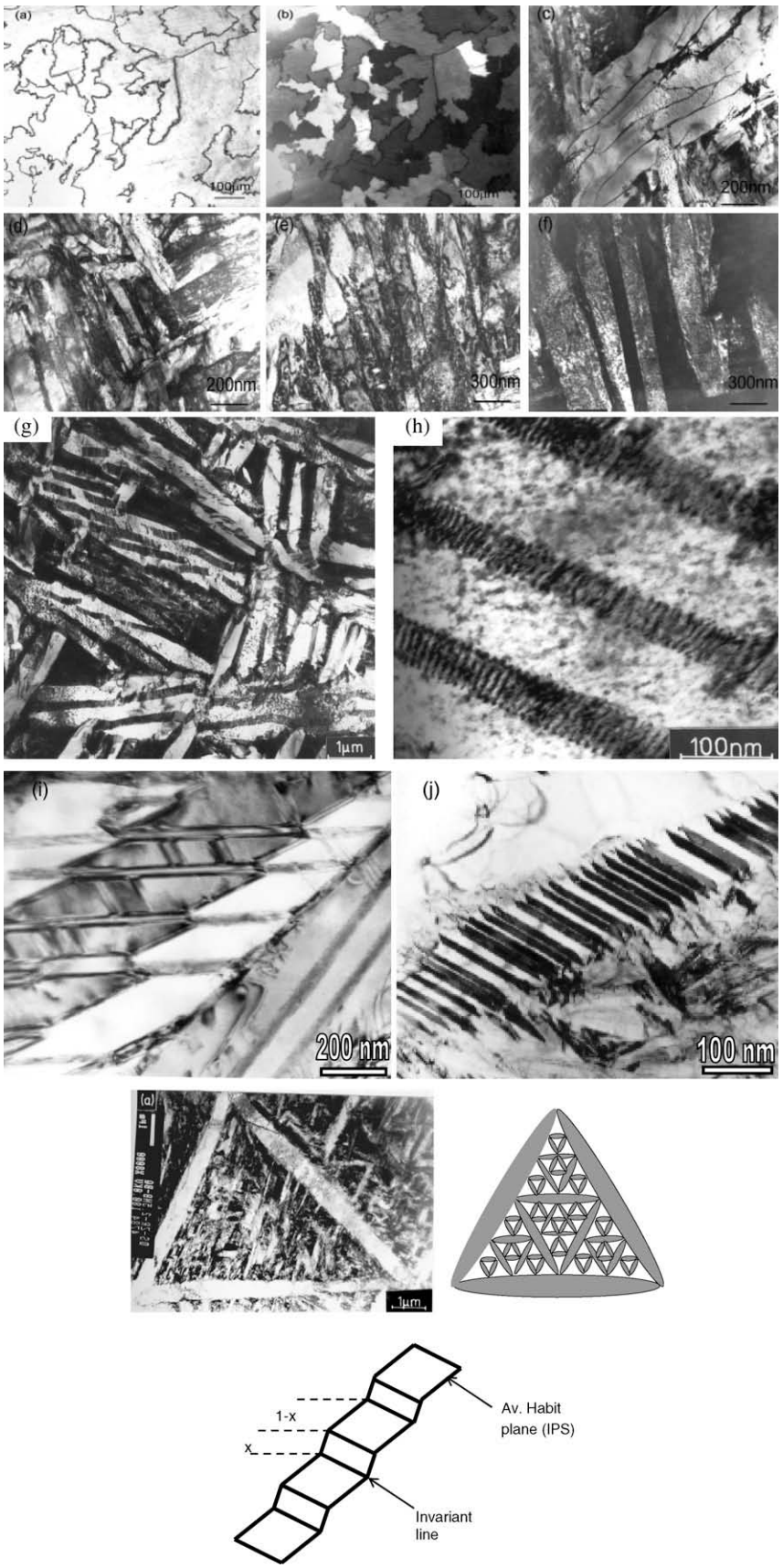

Fig. 2. Various morphologies of martensite. (a) and (b) Massive martensite formed on quenching iodide pure zirconium from the β-phase field. (c) Packets of laths in a Zr–15% Nb β-quenched alloy showing irregular lath to lath interfaces. (d) β-quenched microstructure of Zr–5.5% Nb alloy. (e) and (f) are bright and dark-field micrographs showing alternately twin related laths in a Zr–2.5% Nb alloy. (i) and (j) Bright field TEM micrographs showing plate martensites (i) internally twined (thick twins) martensites (j) internally twined martensite where the minor twin fraction is very thin. (k) Microstructure of the beta quenched sample of Zr–2.5% Nb alloy showing arrangement of primary and secondary plates (l) schematic presentation of the plate arrangements shown in (i–k).

exhibit such lath morphology are all associated with high M_s temperatures (above 923 K) and the reported habit plane indices in these lathe is close to {3 3 4} [21–24]. The packets of the twin related laths are encountered more frequently in alloy such as Zr–2.5% Nb [20] in which the M_s temperature is brought down close to 923 K (Fig. 2(g)).

The plate morphology is characterized by acicular plates forming along different variants of the habit plane, continuously partitioning β-grains (e.g., Fig. 2(k)). The first generation plates spans across the entire grain of the parent phase. The partitioned grain is then further partitioned by the second generation plates which are shorter in length and the process continues till the transformation is nearly complete (Fig. 2(l)). Detailed crystallographic analysis revealed that $10\bar{1}1$ twinning is frequently observed within these plates. Internally twinned martensite plates could be grouped into two classes. The first group was characterized by an average spacing of thick $10\bar{1}1$ twins where the ratio of the thicknesses of the minor and the major twins was seen to be 1:4, a value which closely matched with that predicted by the phenomenological theory (Fig. 2(i)) [24,25]. The second group of plates was characterized by the presence of very thin twins stacked within the plates (Fig. 2(j)), where the average value of the ratio of the thicknesses of the minor and the major twin variants being much smaller compared to that predicted from the phenomenological theory.

An analysis of habit plane variants of the two types of internally twinned plates indicates that there exists an important difference between them in terms of the orientations of their minor twin components. In Bowles–Mackenzie theory [25], four nonequivalent habit plane solutions, denoted by (α± ω±), are obtained. For the given lattice correspondence and for the lattice invariant deformation on the $(1\bar{1}01)$ plane, the orientation relations corresponding to the (α− ω+) and the (α+ ω+) solutions, as shown in stereogram in Fig. 3, are generated by a rigid body rotation around the [0 0 0 1] direction in either the clockwise or the anticlockwise direction. The most important difference between these two solutions arises from the fact that the $(1\bar{1}01)$ plane (on which the lattice invariant shear (LIS) acts) remains nearly parallel (<2°) to the (0 1 1) mirror plane in the case of the (α− ω+) solution whereas it gets separated from the (1 1 0) plane by an angle of about 11° for the (α+ ω+) solution. In the case of a plate which belongs to the (α− ω+) solution, both the twin components follow the Burgers orientation relation very closely and, therefore, each twin component nearly satisfies the invariant plane strain (IPS) condition. As a consequence, these two twin components can grow to a significant extent (the thickness of the minor twin variant >100 nm), maintaining independent habit plane segments with the parent phase.

In the (α+ ω+) case, the twin plane $(l\bar{1}01)$ does not remain parallel to the (1 1 0) mirror plane following to the rigid body rotation. The major twin fraction in this case though satisfies the Burgers orientation relation and the IPS condition quite closely, the minor twin fraction does not obey the IPS condition [3]. The growth of such a variant would cause a substantial buildup of strain, resulting from the deviation from the IPS condition. This would restrict the growth of the minor twin fraction. The observed stack of very thin twins in the martensite plates belonging to the (α+ ω+) solution lends support to this contention. Since the requirement of LIS is not met in these plates in which the twin thickness ratio is much smaller than the predicted value of 1:4, the operation of an additional component of lattice invariant shear in the form of slip appears essential. A periodic array of $\langle c + a \rangle$ dislocations along a different variant of $10\bar{1}1$ planes within minor twin fraction is suggestive of the additional lattice invariant deformation.

2.2. Athermal $\beta \rightarrow \omega$ transformation

With increasing concentration of the β-stabilizing elements in Zr alloys, the β → ω transformation has been found to prevail over the martensitic transformation. Upon quenching from the β-phase field alloys, having composition in the range where martensite start temperature is lower than the ω-start temperature ($M_s(\omega)$), undergo the athermal β → ω transformation (Fig. 1). The athermal nature of the transformation has been established through ultra-high quench rate (~11 000 K/s) experiments [26]. The complete reversibility of the transformation is another evidence for its athermal nature. All these observations suggest that this transformation can be classified as a displacive transformation.

The morphology of the athermal ω-particles is generally ellipsoidal with particles aligned along one of the $\langle 1\,1\,1 \rangle_\beta$ directions. Fig. 4(a) shows a dark-field micrograph taken from the $1\bar{1}00$ reflection pertaining to the ω structure. The typical size range of the ω-particles is 2–10 nm with a separation between the particles being of the same order. A nearly homogeneous distribution of ω particles can be observed in the micrograph. Such a morphology of the ω-phase is different from the plate-like morphology (a characteristic feature of a martensitic transformation) and, therefore,

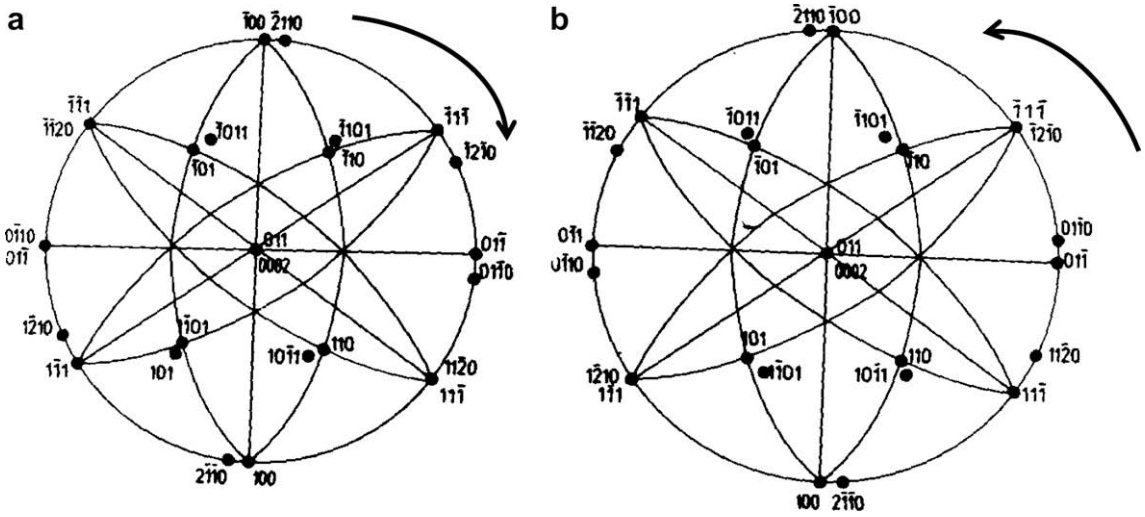

Fig. 3. Stereographic projection showing the orientation relations corresponding to the two solutions of Bowles and Mackenzie formulation (α − ω+) and (α+ ω+). These two orientations are derived from (a) the clockwise and (b) anticlockwise rotations along $[1\,1\,0]_\beta || [0\,0\,0\,1]_\alpha$.

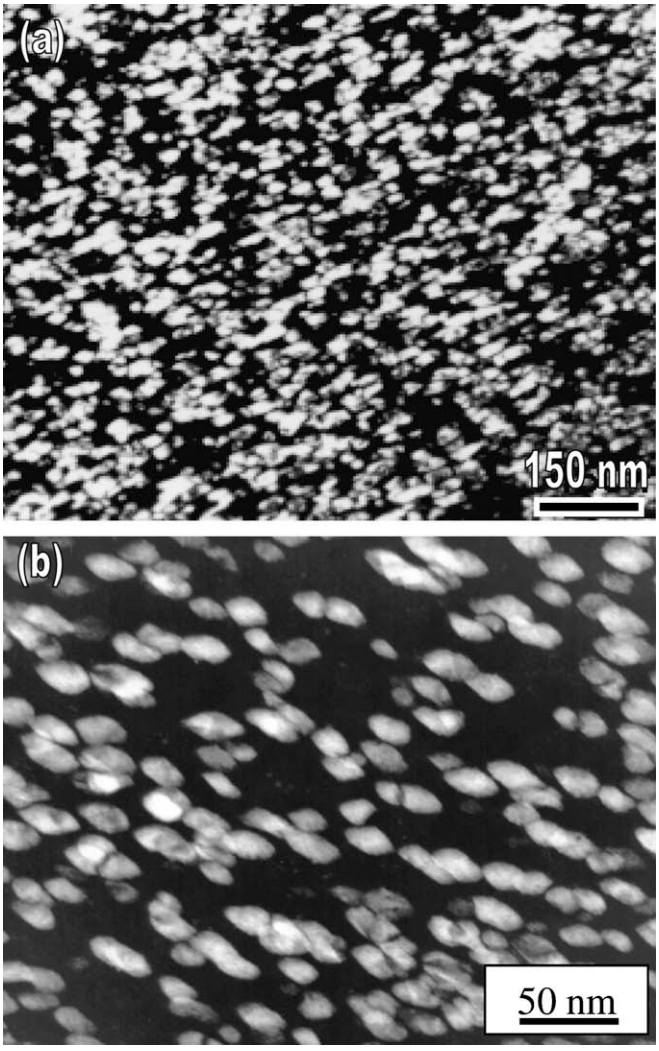

Fig. 4. Various morphologies of the ω-phase. (a) Dark-field micrograph ($\mathbf{g} = 1\bar{1}00_{\omega}$) of a Zr-based alloy showing the arrangement of the ellipsoidal ω with major axes of the particles aligned along $\langle 111\rangle_{\beta}$. (b) Dark-field micrograph ($\mathbf{g} = 1\bar{1}00_{\omega}$) of a Zr-based alloy showing the arrangement of the cuboidal ω with edges of cuboids aligned along $\langle 100\rangle_{\beta}$.

the athermal $\beta \rightarrow \omega$ transformation is not categorised as a martensitic transformation in spite of its athermal and composition – invariant character. The observed orientation relationship between the β and the ω-phases can be represented as [27]

$$111_{\beta}//(0001)_{\omega};\quad \langle 1\bar{1}0\rangle_{\beta}//\langle 11\bar{2}0\rangle_{\omega}$$

As evident from this orientation relationship four variants of the ω-phase are possible and within a given field of view all variants have equal probability to form.

Plate like morphology, akin to the martensitic plates, of the ω-phase has also been encountered when Zr and its alloys subjected to dynamic high pressure loading. The habit plane between the ω-phase and the β-phase was found lying close to $\{112\}_{\beta}$ (Fig. 4(b)). As the duration of the shock loading is typically of the order of few μs, diffusive atom movement is negligible. Hence the shock loading experiment, in a sense, is synonymous to the athermal treatment. The plate-shape morphology, therefore, is representative of the shear-dominated process and therefore, the habit planes of the ω plates are predictable on the basis of phenomenological theory of martensite crystallography. Detail crystallographic analysis revealed that the underlying mechanism

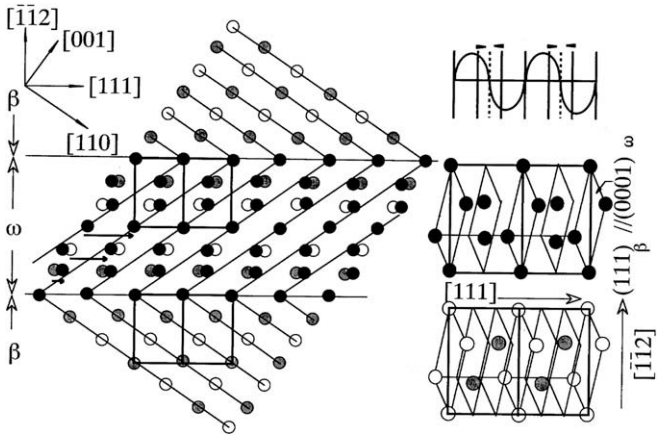

Fig. 5. Schematic presentation of the bcc structure. The $1\bar{1}0$ plane is parallel to the plane of the paper. A combination of the shear and shuffle produces the ω lattice in the bcc lattice. Equivalence between the shear mechanism and displacive wave mechanism is also shown in the figure.

is shear dominating in this case [18,28]. Fig. 5 shows that a macroscopic shear on the $\{112\}_{\beta}$ plane along a $\langle 111\rangle$ direction, superimposed with atomic shuffles, can produce the ω structure. The lattice correspondence between the β and ω lattices remains the same as that encountered in the case of as quenched samples. Since any specific {112} plane contains only one $\langle 111\rangle_{\beta}$ direction, a single orientational variant of the ω structure can be produced within a single {112} plate.

In short, the deformation produced by a shock wave in the bcc lattice develops a tendency for the shear of the {112} planes where the formation of the ω structure occurs when the shuffle process is superimposed on the shear deformation. The axis of the shear direction decides the choice of the variant for the $\langle 111\rangle$ direction contained in the specific {112} plane and, therefore, plate-shaped single variants of the ω-phase emerge in the shock deformed β-phase.

3. Diffusional transformations

On aging Zr-based alloys often exhibits the formation of new metastable/stable phases which have structural relationship with the parent phase. The sequence of the phase transformations in some alloys is influenced by the presence of the miscibility gap observed in the β-phase and the sequence of the phase transformation can be predicted by the relative positions of the free energy curves in the free energy versus composition (G–x) plots.

3.1. Tempering of martensite

On tempering, the martensitic α′-phase decomposes to produce a distribution of the β-phase. The miscibility gap in the β-phase observed in the Zr–Nb phase diagram plays an important role in deciding the phase transformation sequence during the tempering of the α + β alloys. Typical microstructures obtained upon tempering are shown in Fig. 6. The most striking observations [29–31] regarding the evolution of microstructures during tempering can be summarized in the following:

(i) The phase, which precipitates in the temperature interval of 773–883 K, is the β_1-phase (Zr rich β) and not the equilibrium β_2-phase (Nb rich β) (Fig. 6(a)–(d)).
(ii) At temperatures below 773 K and above 883 K, precipitation of the equilibrium phases, β_2 and β_1, respectively, takes place during tempering of the Zr–2.5% Nb martensite.

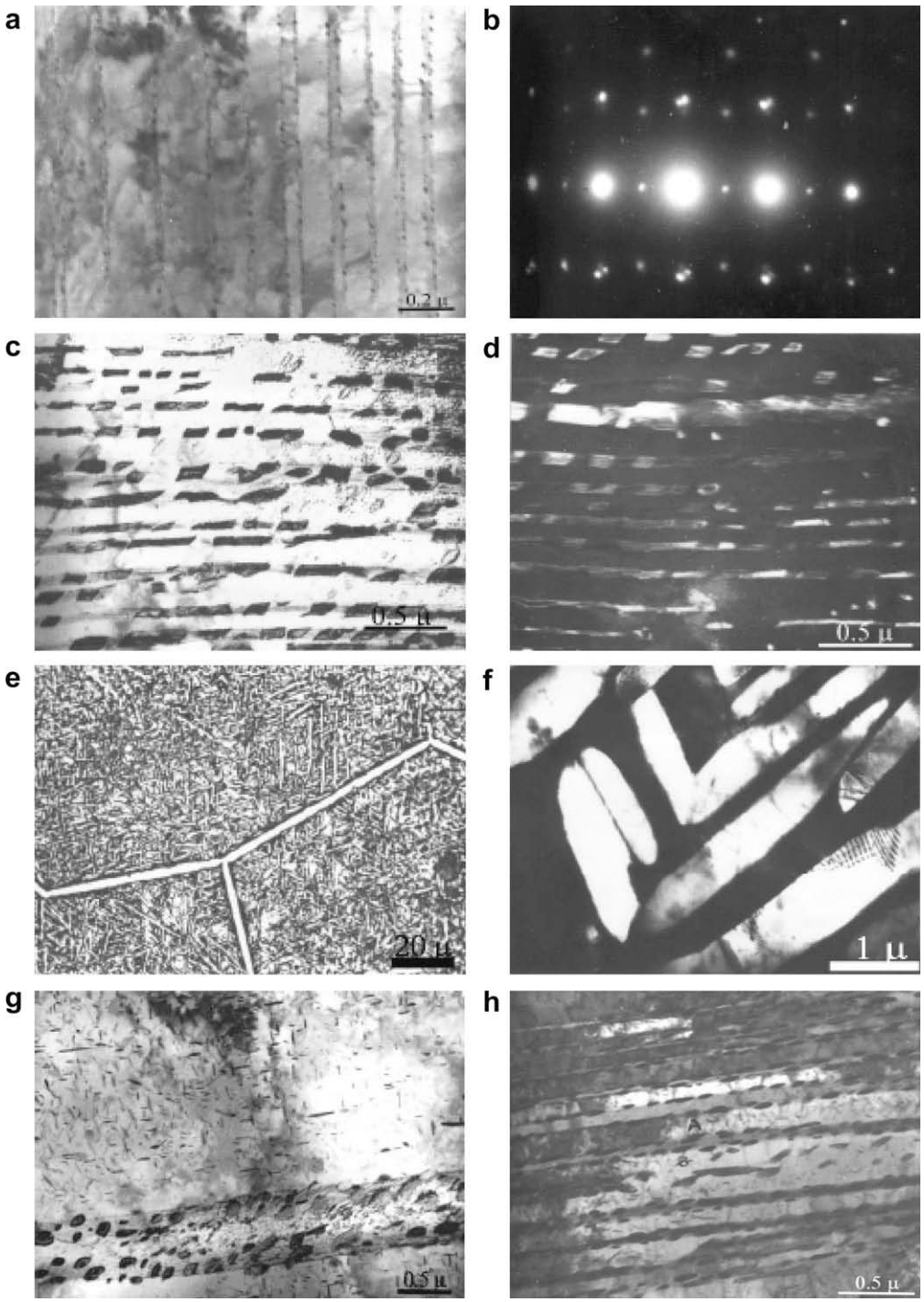

Fig. 6. (a) β_2 precipitation along the twin boundaries in internally twinned martensite plates in Zr–2.5 Nb upon tempering at the temperature of 773 K. (b) SAD pattern showing superimposition of reciprocal lattice sections of two twin related α and the precipitate β_1 orientations. (c) and (d) β_1-phase precipitation at the tempering temperature of 823 K, the dark-field image (d) is taken with a $\{1\,1\,0\}_\beta$ reflection. (e) Light and (f) TEM micrographs showing α-grain boundary allotriomorphs at coarse β-grain boundaries and fine α plates within the β grains in the Zr–5.5% Nb martensite tempered at 823 K. The formation of the coarse β grain structure indicates reversion of α′ martensitic into β which subsequently decomposed into a structure consisting of α plates within β grains and α-allotriomorphs at β grain boundaries. (g) Twin boundary β_1 precipitates and needle shaped β_2 precipitates within martensites plates in the tempered Zr–2.5 Nb alloy. (h) TEM micrograph showing the morphological evolution of β_1 precipitates at $10\bar{1}1_\alpha$ twin boundaries of Zr–2.5Nb martensite during tempering. The orientation of the twin boundary β_1 precipitates is the same as that of the parent β-phase. α laths are $10\bar{1}1$ twin related.

(iii) On tempering, the Zr–5.5% Nb martensite initially reverts back to the parent β-phase via a composition-invariant process; subsequently the reverted β-phase transforms into a structure consisting of Widmanstatten α-plates in a β_1-matrix (Fig. 6(e)–(f)).

Free energy–composition (G–x) plots have been used to rationalize these observations [31]. The G–c plots in Fig. 7 represent typical free energy curves for the α- and the β-phases for temperatures lower than T_{mono}. Banerjee et al. [31] have shown that relative positions of the common tangents between the α and the β_1

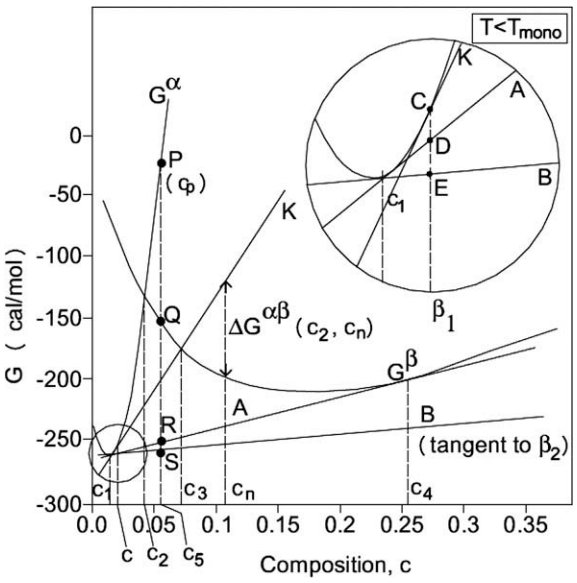

Fig. 7. Free energy-concentration plots for the α and the β-phases in the Zr–Nb system at 850 K showing that a metastable equilibrium (represented by the common tangent A) can be established between the α and the β_1-phase. See text for transformation sequences for alloys having compositions c and c_5.

(shown as line A in Fig. 7) and α and β_2 (shown as line B in Fig. 7) indicate the metastable and stable equilibrium between the α on one side and the β_1 and β_2 on the other. The strong preference for the formation of β_1 precipitates during tempering at the temperature range, 773–883 K, has been explained in terms of the compositional barriers associated with the nucleation of the β_1 and the β_2 precipitates and role of the miscibility gap in providing higher energy barrier for the β_2 precipitation. For example, the chemical free energy change, $\Delta G^{\alpha\beta}(c, c_n)$, accompanying the nucleation process for β_1 nuclei (with composition given by c_n, shown in Fig. 7), is negative when $c_n > c_3$. Such β-nuclei will continue to get enriched with Nb and the free energy will follow the G_β curve. During the process of Nb enrichment the β-nuclei composition will attain the level, c_4, where the common tangent between the G_α and $G_{\beta 1}$ curves meets the G_β curve. A metastable equilibrium between the matrix α and the β_1-phase is established at this point. A further Nb enrichment of the β-nuclei to approach the composition level corresponding to the β_2-phase is hindered by the presence of a large free energy barrier in the G_β curve.

In case of supersaturated martensite with a composition $c > c_2$ (Fig. 7), tempering at 850 K can cause a reversion from α′ to β. The thermodynamic feasibility of a composition-invariant α′ → β transformation is shown for the α′ composition c_5 by the vertical drop in the free energy from P to Q. In a subsequent step the β-phase decomposes into a mixture of α + β_1-phase mixture (metastable) and finally into the equilibrium α + β_2 structure. The overall transformation can then be described by the following scheme:

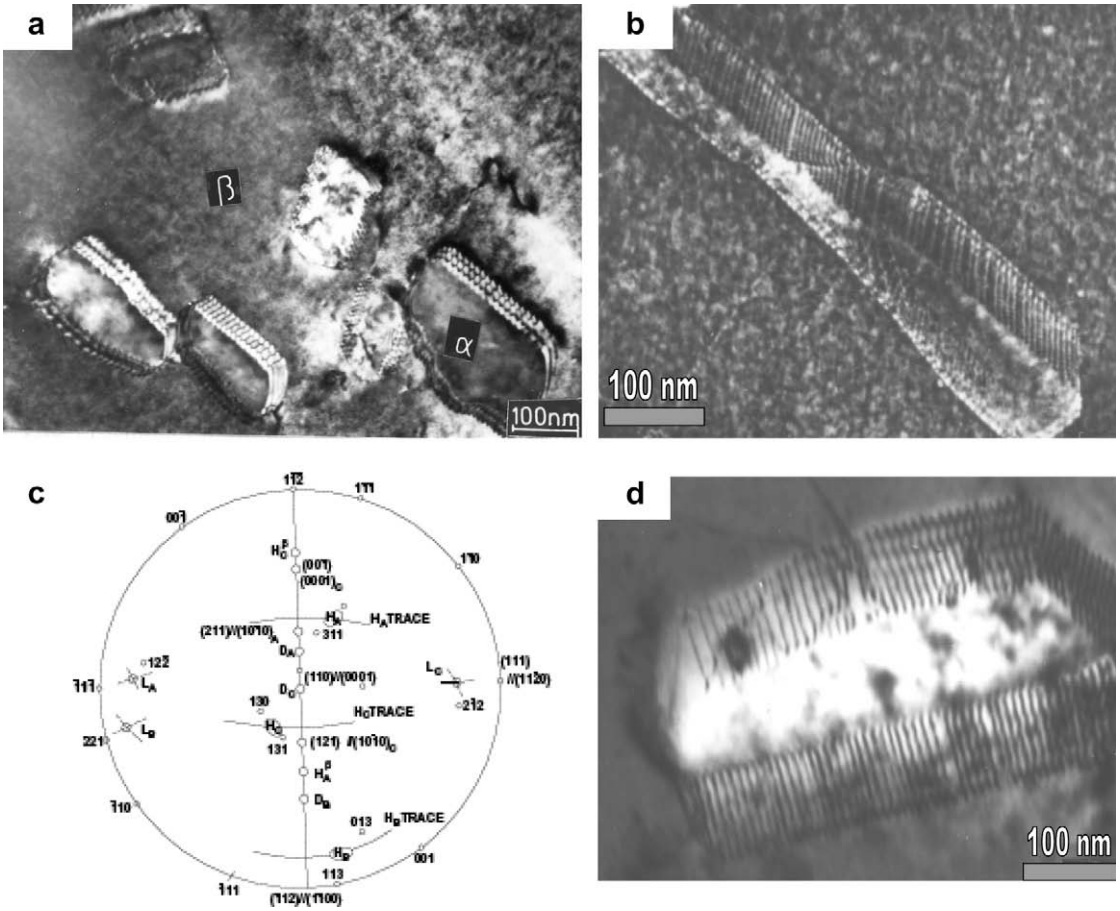

Fig. 8. (a) Several variants of α precipitate laths in the β-matrix of the Zr–20% Nb alloy. All variants exhibit arrays equispaced dislocations lined up along the length of the precipitates. (b) Interfacial (αβ) dislocations, with line vectors parallel to the long direction of the precipitates. (c) Equispaced ⟨c + a⟩ dislocations at α/β interfaces lying along the long direction of this precipitate plate. (d) Stereogram showing that three variants of orientation relationship are operative for three habit variants of precipitates shown in (a).

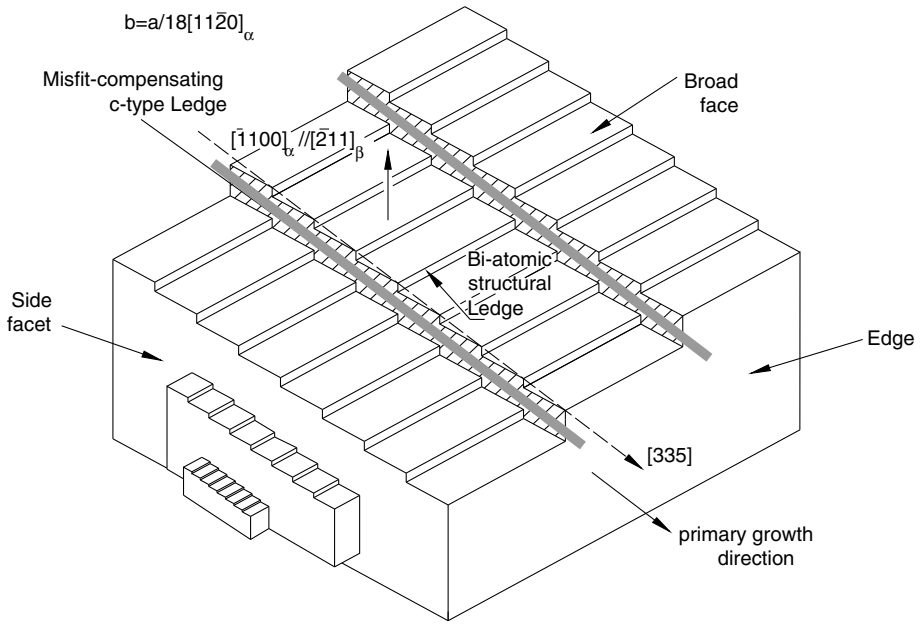

Fig. 9. Schematic presentation of the interfacial illustration of the interfacial structures of α plates growing in β-both the broad face and the side fact are shown.

$$\alpha'(c_5) \rightarrow \beta(c_5) \rightarrow \alpha + \beta_1 \rightarrow \alpha + \beta_2$$

Drops in free energy for this sequence are shown by the vertical segments, PQ, QR and RS.

With decreasing temperature, the β_1 arm of the G_β curve goes up with respect to the G_α curve and below a certain temperature limit, ($T < (T_{mono} - 100\ K)$), it is not possible to construct a common tangent between the G_α curve and the β_1 portion of the G_β curve. In such cases direct nucleation of the β_2-phase takes place during tempering. This process involves the overcoming of a very large free energy barrier and hence the reaction is expected to be very sluggish as is indeed the case. Luo and Weatherly (1988) have studied the precipitation behaviour of the Zr–2.5% Nb alloy and have confirmed that both β_1 and β_2 precipitates form in this alloy during tempering. The rationale of the formation of bcc precipitates of two widely varying compositions (β_1: Zr–20% Nb and β_2: Zr– 85% Nb) at temperatures close to but below the monotectoid temperature has been corroborated by their studies. They have also pointed out that the precipitate phase forming at 773 K is exclusively β_2 while both β_1 and β_2 precipitates form at 873 K. For the latter treatment, homogeneously nucleated precipitates within the martensite plates have been identified to be of the β_2 type and the twin boundary nucleated precipitates are invariably of the β_1 type. The crystallography of precipitation of β_1 and β_2 phases has been studied by Banerjee et al. [31] and Luo and Weatherly [29] which not only support these arguments but also show that the β_1 and β_2, both show relationship close the Burger relations with the α phase. It has also been shown that the orientation relation obeyed by the needle shaped β_2 precipitates is consistent with the ILS condition and the growth direction of these needles is very close to the ILS direction.

3.2. Precipitation of α in the β-matrix

The Zr–2.5% Nb alloy has been processed or heat treated in the α + β-phase field in such a manner that the α-phase is precipitated in the β-matrix. Such microstructures show precipitates of the α-phase in the form of plates which maintain strict orientation relation and habit plane with the β-matrix. The presence of features like orientation relationship, habit plane and sometimes surface relief does not necessarily suggest that a lattice shear mechanism is operative. It has been shown that a diffusional transformation in which lattice site correspondence is maintained between the parent and the daughter phase, also exhibits orientation relationship, habit plane and shape deformation [32]. Laths or needles of the product phase in a diffusional transformation grow along the invariant line of the transformation with the orientation relationship being determined by the restrictions imposed by the invariant line criterion [33,34].

The interface structure of α-laths in the β-matrix has been studied in Zr–Nb alloys by Perovic and Weatherly [35] and by Banerjee et al. [36]. In the Zr–2.5% Nb alloy, in which the volume fraction of

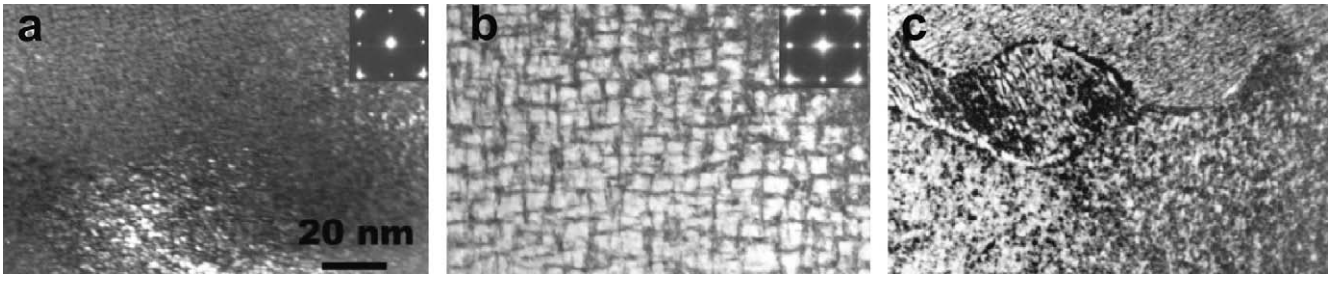

Fig. 10. Cuboidal morphology of the ω related phase. (a) The cuboidal morphology in the initial stages could be noticed; also the streaking in the SAD pattern along ⟨100⟩ directions shown in inset. (b) The increase in the size of Cuboid and also the alignment along ⟨100⟩ directions could be noticed. (c) Presence of the cuboidal shape omega phase in several grains could be noticed.

the β-phase is rather small, the α/β interfaces have been shown to contain an array of straight and parallel 1/3 $\langle 11\bar{2}3\rangle$ (or $\langle c+a\rangle$) dislocations with spacing of about 6–8 nm at the interfaces (Fig. 8). These dislocations have been found to lie along the common $(101)_\beta||(\bar{1}011)_\alpha$ plane. In addition to these, some 1/3 $\langle 11\bar{2}0\rangle$ (or $\langle a\rangle$) dislocations have been observed to lie both parallel to and across the $\langle c+a\rangle$ dislocations. The density of the $\langle a\rangle$ dislocations has been found to increase with increasing rotation of the α/β interface from the flat facets where only one set of $\langle c+a\rangle$ dislocations is present. Because of the irregularity of the α/β surface in the Zr–2.5% Nb alloy an accurate determination of the habit plane has not been possible. However, the line vectors of the $\langle c+a\rangle$ dislocations have been identified to be the direction of the invariant line strain.

In the Zr–20% Nb alloy, laths of the α-phase formed on isothermal treatment at 823 K with the length varying from 200 to 1000 nm. Several variants of α- laths are often encountered in a single field of view; a typical example is depicted in Fig. 8(a). Orientations of all the variants match the Burgers relation quite closely. The α/β interfaces of these laths have invariably been found to contain arrays of parallel, equispaced dislocations of $\langle c+a\rangle$ type Fig. 8(a) and (b). The spacing between adjacent dislocations varies from 8 to 10 nm. The habit plane of these laths has been found to lie between the $\{103\}_\beta$ and $\{113\}_\beta$ poles (Fig. 8(c)) and the line vectors of the $\langle c+a\rangle$ dislocations at the interface are along the $\langle 334\rangle_\beta$ directions which match closely with the invariant line. The observations on the morphology, orientation relation and crystallography of α-laths forming from the β-phase in a diffusional process can be summarized as follows:

(a) The orientation relation between the β and the α-crystals is very close to the Burgers relation.
(b) The habit plane is an irrational plane. Habit plane poles of different variants are found to lie between the $\{103\}_\beta$ and $\{131\}_\beta$ poles. For all the variants of laths, habit planes remain close to the α/β conjugate pair $01\bar{1}0_\alpha||\{112\}_\beta$ along which registry between atomic planes can be achieved by presence of structural ledges.

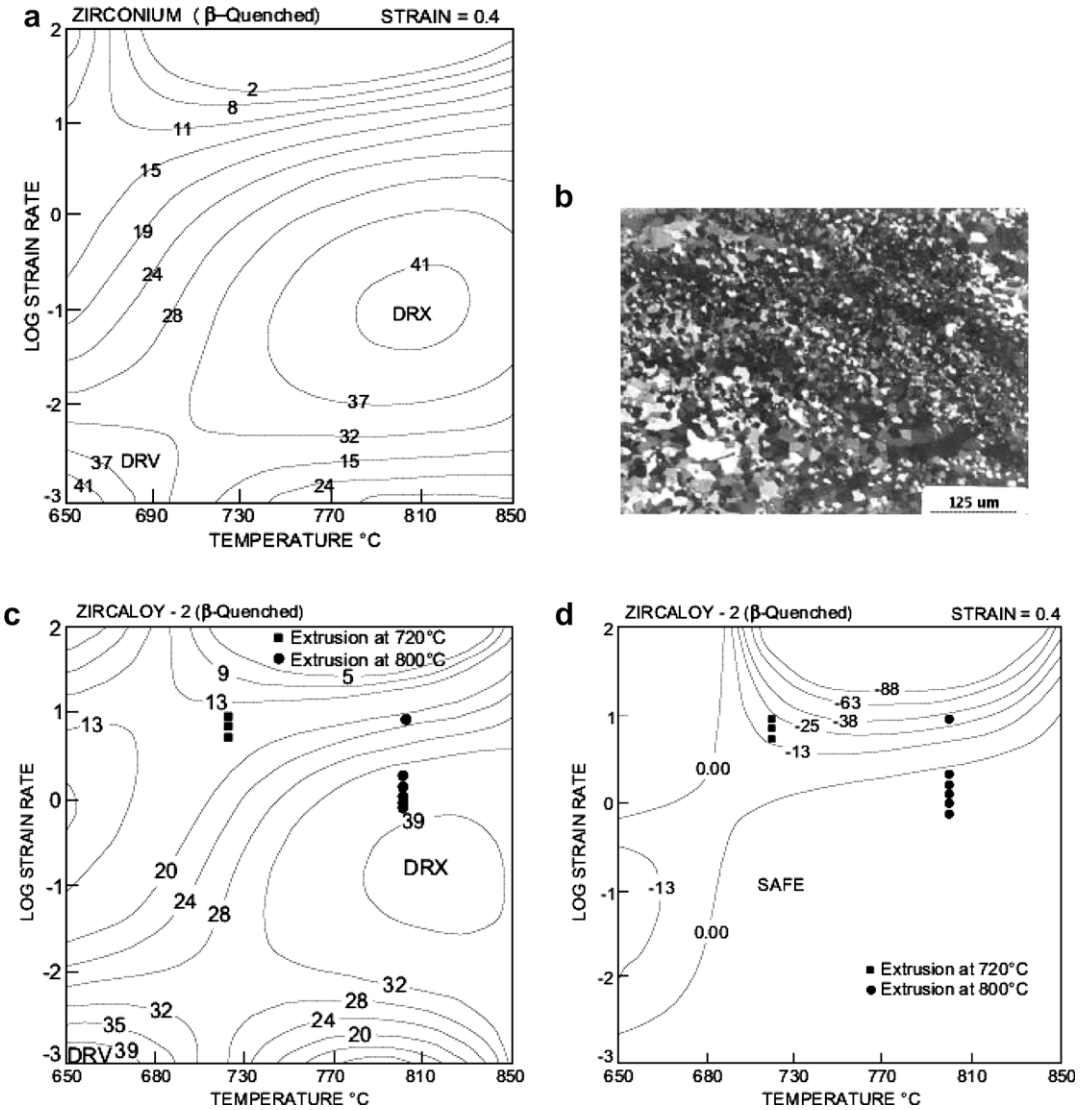

Fig. 11. (a) Processing map for zirconium for a strain of 0.4 showing domains of dynamic recrystallisation (DRX) and dynamic recovery (DRV). The number against each contour indicates percentage efficiency. (b) The optical micrograph of α-Zr deformed at 1073 K and 0.1 s^{-1} within the DRX domain to a strain of 0.7 showing dynamically recrystallized grains. (c) Processing map of β-quenched Zircaloy-2 for a strain of 0.4 showing various domains marked as DRX, DRV and SPD (domain of super plasticity) (d) Extrusion conditions superimposed on instability map of β-quenched Zircaloy-2 for a strain of 0.4. The extrusions carried out at 1073 K are in the stable flow regime while those carried out at 993 K are within the instability regime.

(c) Interfacial dislocations with $\langle c + a \rangle$ Burgers vector remain aligned along the invariant line and are arranged in a parallel array with a spacing of about 8–10 nm (Fig. 8(b)).
(d) The long direction of laths matches closely the invariant line direction $\langle 433 \rangle_{\beta}$.

Experimental and theoretical work on the nature of α/β interfaces in diffusional transformation products of many alloy systems has proved that there exists a good coherency between the bcc matrix and the hcp product across the interface [37–39]. The presence of coherency at the transformation front is suggestive of a lattice site correspondence which produces a shape strain in some diffusional transformations. A comparison between the interfaces/transformation fronts in martensitic transformations and these diffusional transformation shows:

(i) Both the types are shown to be irrational and usually partially coherent. Fully coherent irrational interfaces are rare, but they are found in some martensitic transformations, e.g., Ti–22 at.% Ta [40].
(ii) Partially coherent interfaces of martensite plates are usually irrational because of the invariant plane strain requirement and the fact that the lattice invariant shear is a simple shear. In contrast, partially coherent irrational interfaces in diffusional transformations are essentially epitaxial, and are made up of terraces of rational interfaces, separated by steps or ledges.
(iii) Interfaces of martensite plates should be necessarily glissile and should conserve the number of atoms during propagation. A new layer of the product phase forms by the migration of a growth ledge in diffusional transformation does not conserve the number of atoms. In general, diffusional transformations involve non-conservative movements of dislocations at the transformation fronts.

Many of the experimental findings on diffusional growth can be explained using Fig. 9 which shows the growth the α phase using ledge mechanism Growth ledges have been observed to contain misfit dislocations on the broad as well as on the side facet of the lath. Such dislocations have sessile orientation and, therefore, it must climb for the motion of the growth ledge riser. Since diffusion and partitioning of alloying elements accompany such a growth process, non-conservative motion of dislocations at the transformation front is facilitated. The broad face of the lath is formed by the coalescence of growth ledges on this surface. This riser plane of growth ledges on the side facet contains the structural ledges and is thus semicoherent. The migration of the growth ledges should occur by the kink on ledge mechanism in which diffusing atoms get attached to the kink plane. Since these ledges do not coalesce to the extent necessary for forming a complete layer on the side facet, the broad face remains as a stepped interface with steps along the lattice invariant line. These steps are nothing but the misfit compensating c-type ledges. The ledge growth mechanism in a diffusional transformation requires (a) atomic diffusion to effect the partitioning of the alloying elements, (b) some mechanism by which new ledges are formed on the newly created layer, and (c) maintenance of the semicoherent interfacial structure. In a steady state, these processes must all conform to the overall rate that is determined by the process which consumes the major part of the driving force.

3.3. Isothermal $\beta \rightarrow \omega$ transformation

Precipitation of the ω-phase occurs in a β-phase matrix of relatively concentrated alloys upon ageing at temperatures below about 773 K, which is the upper cut-off temperature for the ω-phase formation by aging in most of the β solid solutions (Fig. 10). The progressive increase in volume fraction and the growth of ω-particles with an increase in the isothermal holding

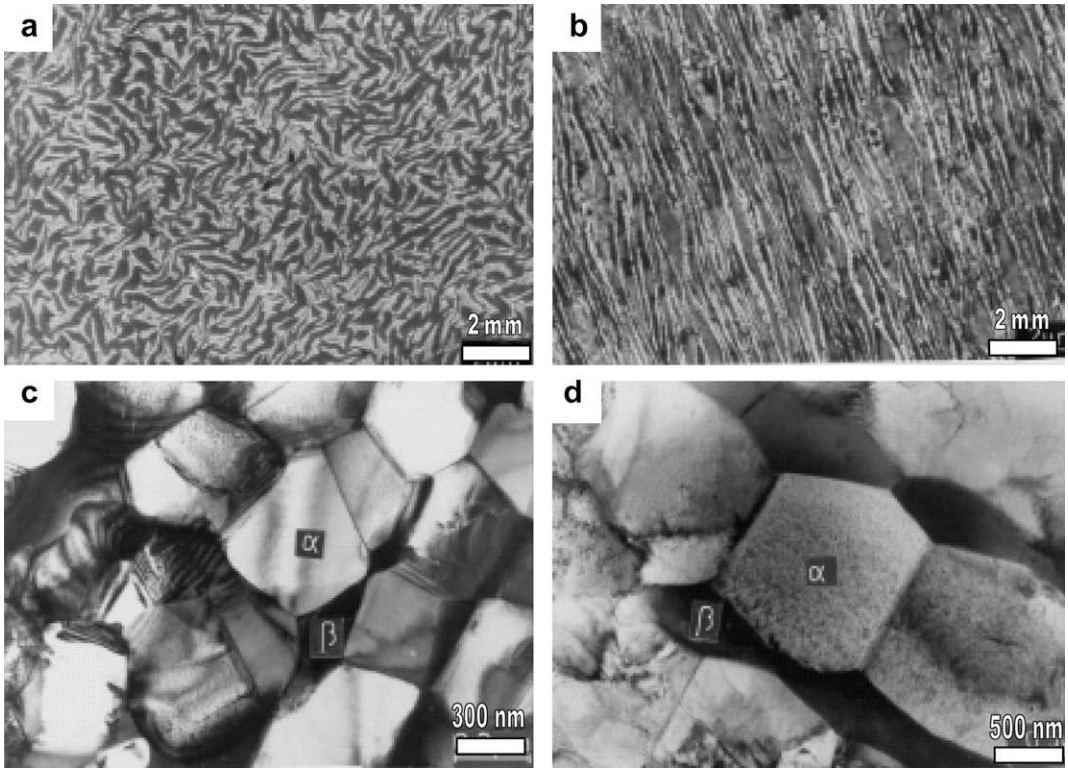

Fig. 12. SEM and TEM micrographs of two phase (α + β) microstructure of hot extruded tube (a) elongated morphology in the longitudinal section (SEM), (b) seriated morphology in the transverse section (SEM), (c) and (d) dynamically recrystallized equiaxed α-grains within α-stringers in longitudinal and transverse sections, respectively (TEM).

time is indicative of a thermally activated transformation mechanism. Time–temperature–transformation (T–T–T) plots pertaining to isothermal ω precipitation have been experimentally generated in several alloys [41]. Both, cuboidal and ellipsoidal ω precipitates result in an isothermal ageing treatment. Fig. 10 shows the typical cuboidal morphology of the aged ω where edges of regularly arranged cuboids are aligned along $\langle 100 \rangle_\beta$. Usually the sizes of the ω precipitates forming by isothermal treatments are in the range of 10–20 nm.

In view of the fact that the β-phase in most of the ω-forming alloys exhibits a tendency for phase separation, spinodal decomposition often precedes the $\beta \rightarrow \omega$-phase transformation during isothermal heat treatments. Spinodal decomposition partitions the β-phase into solute-rich and solute-lean regions and composition modulation occurs only in elastically soft $\langle 100 \rangle$ directions. The morphology of the ω-phase, therefore, is controlled by the $\langle 100 \rangle$ concentration modulation and in the same configuration the ω particles decorate the structure the bcc matrix [42]. Under special circumstances where strain associates with the transformation, ω particles assume ellipsoidal morphology and particles remain small in size due to the transformation strain.

3.4. Microstructural evolution during thermo-mechanical treatments

Zr alloys are mainly hot worked in the (α + β) phase field [43,44]. A difference in crystal structure, coupled with a very high diffusivity in the β-phase (2–3 orders of magnitude higher than that in the α-phase), promotes the processes of recovery, recrystallization and diffusional transformation at lower temperatures and higher strain rates in the β-phase as compared to the α-phase. Consequently, the constitutive deformation behaviours of these phases under hot working conditions are different and this dictates the evolution of microstructure in the product.

In addition to dynamic recovery (DRV) and dynamic recrystallization (DRX), superplastic deformation has also been reported in Zr alloys by McQueen and Bourell [43]. Structural changes can also occur during the intervals of hot working in the absence of stress (static) as well as during cooling after hot working [43]. Zr alloy systems are also known to exhibit strain localization leading to non-uniform microstructures during deformation processing.

Jonas and co-workers [45,46] studied the high temperature deformation behaviour of α-Zr and α-Zr–Sn alloys in compression and concluded that dynamic recovery has occurred in the temperature range, 898 to 1098 K and the strain rate range, 10^{-4} to 3×10^{-3} s^{-1}. Although the deformation was carried out at or above the recrystallization temperature (static), no recrystallized grain has been observed in the deformed material. On the other hand, Ostberg and Attermo [13] carried out forging of Zircaloy-2 (a near α alloy) at 1073 K and at a strain rate of 0.4 s^{-1}, and observed that the original Widmanstatten α plates were broken up into new grains which were equiaxed. They concluded that DRX was involved in the modification of the microstructure. Garde et al. [12] studied hot tensile deformation behaviour of Zircaloy-2 in the two phase (α + β) field at various strain rates. The microstructure evolved during deformation at temperatures around 1123 K and lower strain rates (<10^{-3} s^{-1}) was characterized by equiaxed α-grains separated by β-phase. The phenomenon of grain boundary sliding has been found to be responsible for the occurrence of equiaxed grain structure.

Chakravartty et al. [15,47–50] studied the hot deformation characteristics of commercial pure Zr (~1000 ppm O) with a β quenched starting microstructure in both α and β-phase fields using processing maps generated by carrying out compression testing in the strain rate range of 10^{-3} to 10^{2} s^{-1} and over the temperature range of 923–1323 K. The processing map revealed (Fig. 11(a)) two safe domains and a regime of instability rate [47–50]:

(i) a domain of dynamic recrystallization (DRX) in the temperature range of 1003–1123 K and strain rate range of 10^{-2} and 0.1 s^{-1},
(ii) a domain of dynamic recovery at temperatures lower than 973 K and strain rates lower than 10^{-2} s^{-1} and
(iii) a regime of flow instability at strain rates higher than 1 s^{-1} and temperatures above 943 K. The manifestation of instability was in the form of localized shear band (Fig. 11(b)). It is to be noted that the regime of instability should be avoided during hot working.

Processing maps of the commercial Zircaloy-2 were also developed. Comparison of the processing maps of Zircaloy-2 and commercially pure Zr in β-quenched condition reveals that the maps are very similar. The DRX domains of both the maps extend over similar strain rate and temperature ranges, although the peak efficiency (38%) for DRX for Zircaloy is slightly lower than that of Zr(42%). In order to validate the processing maps of Zircaloy-2, extrusion trials have been carried out on full size billets and ingots used for making various Zircaloy-2 products for nuclear reactor use. Two different temperatures (993 and 1073 K) and various extrusion ratios and ram speeds were chosen [47]. The experimental extrusion conditions were located on both the processing map (Fig. 11(c)) and instability map (Fig. 11(d)). Most of the extrusions carried out at 1073 K are within the DRX domain and the extrusions carried out at 1003 K fall in the instability regime. The extrusion carried out at 1003 K showed dynamically recrystallized grains while the microstructure of extruded material depicted signs of flow localization [15,47–50].

The fabrication schedule of Zr–2.5% Nb pressure tubes involves hot working of the ingot in the (α + β) phase field either by forging

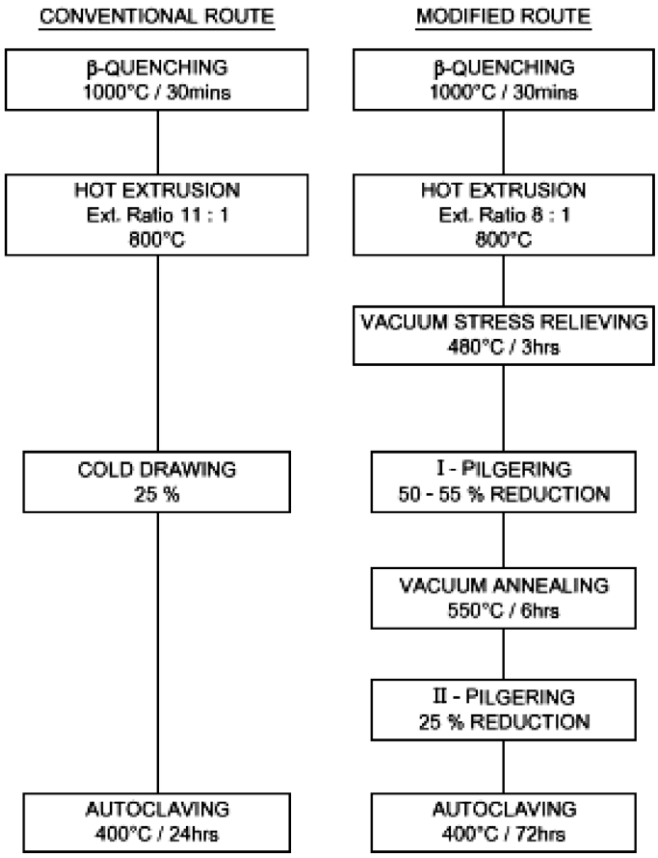

Fig. 13. The conventional and modified fabrication flow sheets of Zr–2.5 Nb alloy Pressure tube.

or by extrusion followed by cold-working steps. The volume fractions of the two phases, and consequently their compositions, the aspect ratios of the α and β-grains and the crystallographic texture of the product are essentially determined by the process parameters of the last hot extrusion step. Fig. 12 shows some typical microstructures of the hot extruded tube in both transverse (Fig. 12(a)) and longitudinal (Fig. 12(b)) directions as revealed by scanning as well as by transmission electron microscopy. SEM photographs show that the two phase (α + β) structure is elongated in the direction of extrusion. The β-phase (bright constituent) stringers are discontinuous and separate the elongated α-phase units. TEM micrographs of both longitudinal and transverse directions reveal that the elongated α-units are essentially made of cluster of nearly equiaxed fine α-grains separated by thin β-phase film (Fig. 12(c) and (d)). This observation suggested the operation of DRX in Zr–2.5% Nb alloy during hot extrusion. In addition to high angle boundaries in the structure, some of the equiaxed grains have also been found to contain sub-boundaries. The combination of high strength with a good ductility and toughness of Zr–2.5% Nb pressure tubes is essentially derived from the fine (α + β) fibrous microstructure consisting of elongated α-grains containing about 0.5% Nb and the β-phase (15–20% Nb) stringers primarily located at α-grain boundaries. Such a structure cannot remain stable if it is subjected to a cold-working–full annealing cycle which tends to coarsen the structure into a distribution of equiaxed α and β grains, resulting in a substantial drop in the ultimate tensile strength.

In recent years, there have been sustained efforts toward improving the resistance to irradiation induced growth (one of the life limiting factors of pressure tubes) through the modification of microstructure of the pressure tube material. In order to improve the properties of the product and produce material which can qualify in terms of microstructure, dislocation density, crystallographic texture and short time mechanical properties as specified for the conventionally processed material, two step cold-working by drawing or pilgering with an optimized intermediate annealing

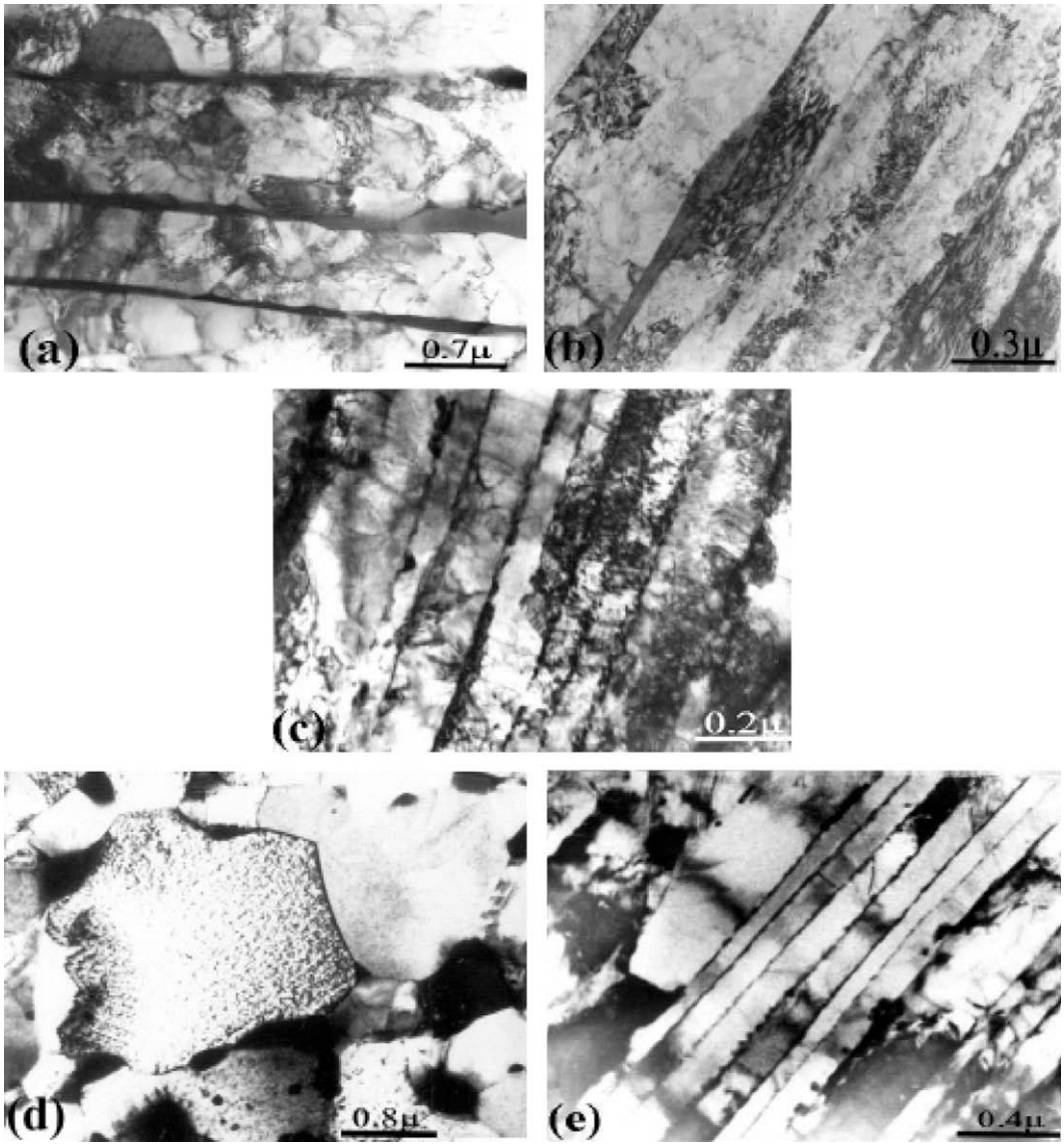

Fig. 14. Transmission electron micrograph of Zr–2.5 Nb alloy (a) as extruded microstructure showing elongated morphology of α-phase separated by β-phase stringers. (b) First pilgered microstructure illustrating the very high dislocation density. The dislocations are concentrated primarily at the α/β interface. (c) Incomplete recrystallization of the α-stringers as evidenced by the presence of a substantial number of dislocations after annealing at 773 K for 6 h, (d) coarsening of the α-grains caused by redistribution and agglomeration of β-phase. The β-phase is located at the triple junctions of α-grains after annealing at 873 K for 1 h and (e) completely recrystallized α-lamellae obtained after annealing at 823 K for 3 h. The lamellar morphology of the two phases is not altered by this annealing treatment.

treatment has been introduced (Fig. 13). Srivastava et al. [3] studied the evolution of microstructure and of tensile properties during each fabrication step of the modified route and compared it with that of the conventional route. The development of microstructure in both the routes was identical during extrusion except the aspect ratio of both α and β grains were lower presumably because of lower extrusion ratio employed and the volume fraction of β_1 was higher owing to faster cooling rate subsequent to extrusion. A typical microstructure in radial–axial section is shown in Fig. 14 which shows elongated α-grains separated by β-phase.

Subsequent to hot working, in the conventional route 20–25% cold work is given to produce a dislocation density of the order of $10^{14}/m^2$ which results in optimum combination of tensile strength and in-reactor creep behaviour (microstructure shown in Fig. 14(b)). The intermediate annealing treatment prior to second pilgering in the modified route has annihilated all the cold work introduced in the first pilgering step so as to get a microstructure and flow properties similar to that obtained after extrusion [3]. Retention of this structure is necessary for obtaining optimum tensile properties at service temperature of 583 K. In their investigation Srivastava et al. [3] have shown annealing treatment at 823 K for 6 h causing nearly complete recrystallization of both the phases without altering the elongated morphology of the $\alpha + \beta_1$ microstructure (Fig. 14(e)) would be optimum for achieving the desired results.

4. Hybrid phase transformations

4.1. Hydride formation

The formation of interstitial compounds, like zirconium hydride, in the matrix can be treated as a process of interstitial ordering where interstitial solutes, which remain distributed randomly in the interstitial sites, assume an ordered array with a lowering of the temperature of the system.

The metastable γ hydride phase, which has an fct structure ($c/a > 1.0$) and can coexist with the α as well as with δ hydride phases, can form at temperatures where any significant self-diffusion of Zr atoms does not occur but interstitial diffusion of H atoms within the time scale of transformation is still possible (cooling rate - 10^4 K/s). Sidhu et al. [51] have shown that the $\alpha \rightarrow \gamma$ transformation involves a shear mechanism. The overall $\alpha \rightarrow \gamma$ transformation process can, therefore, be viewed as a shear transformation of the hcp lattice of Zr atoms with an accompanying H redistribution and interstitial ordering.

The γ hydride phase can also form in the matrix of β stabilized alloys [52–54]. In α + β alloys, H is partitioned between the two phases. Since the solubility of H in the β-phase is much more than that in the α phase, precipitation of hydrides in α + β alloys is encountered more frequently in the α phase and along α/β boundaries than in the β-phase. The γ-hydride phase precipitates form in both the α and the β alloys at high quenching rates.

The characteristic features of γ hydride precipitation, namely, (i) surface relief on polished surfaces, (ii) strict orientation relationship and habit plane, (iii) operation of the invariant plane strain condition, (iv) periodic internal twinning and (v) rapid transformation kinetics, suggest that the transformation involves a lattice shear. Some of these features (Fig. 15) of γ hydride precipitates in the α matrix are shown in Fig. 15. Considering these characteristic features, the γ-hydride precipitation can be grouped in the class of Bainitic transformation.

Based on the observed orientation relations between the γ hydride and the α and the β-phase matrix, Dey et al. [52,53] have proposed the following lattice correspondence (as shown in Fig. 16)

$$[1\bar{1}0]_\beta \| [0001]_\alpha \| [111]_\gamma; \quad [00\bar{1}]_\beta \| [11\bar{2}0]_\alpha \| [10\bar{1}]_\gamma;$$
$$[110]_\beta \| [1\bar{1}00]_\alpha \| [1\bar{2}1]_\alpha$$

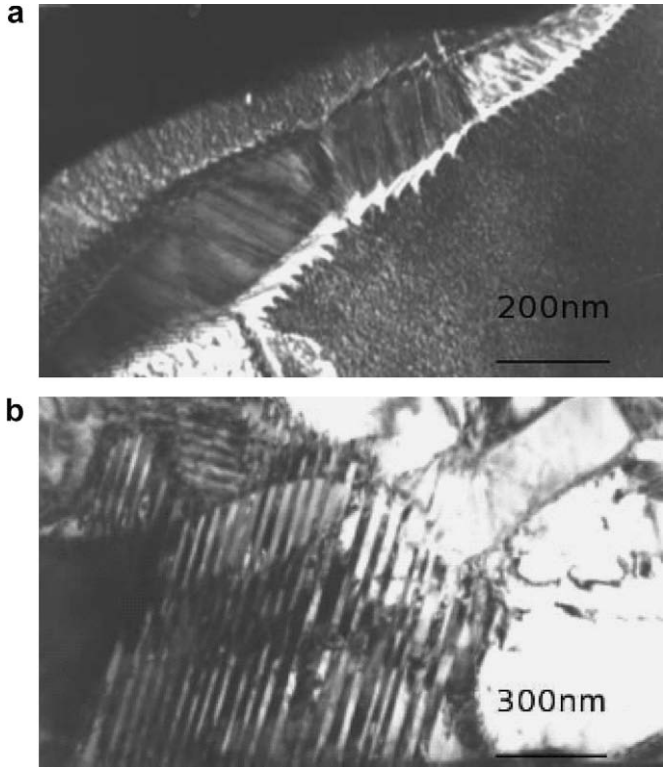

Fig. 15. Micrographs showing γ-hydride in (a) α and (b) β-phase.

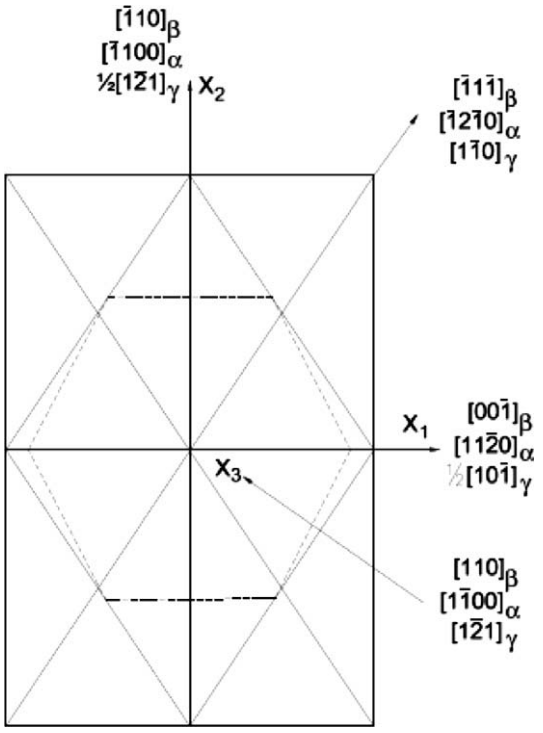

Fig. 16. Lattice correspondences between α, β and γ-hydrides.

While studying the precipitation of γ hydride from the α phase, Weatherly [55] has noted γ hydride precipitates of two distinct classes:

(a) Type I γ hydride precipitates with $10\bar{1}7_\alpha$ habit plane and the orientation relationship:

$$(111)_\gamma||(0001)_\alpha; \quad [1\bar{1}0]_\gamma|||[\bar{1}2\bar{1}0]_\alpha.$$

(b) Type II γ hydride precipitates with $10\bar{1}0_\alpha$ habit plane and the orientation relationship:

$$(001)_\gamma||(0001)_\alpha; [1\bar{1}0]_\gamma|||[1\bar{2}10]_\alpha.$$

The lattice correspondences for both type I and type II γ plates could be regarded as crystallographically equivalent if one considers the α to γ transition to have two components: the first being the α to β transition in accordance with the Burgers correspondence and the second being responsible for converting the β structure to the γ hydride structure.

In view of the close lattice correspondence of the α, the β and the γ-structures, the fact that hydrogen is a strong β stabilizer and the crystallographic observations reported by Dey and Banerjee [53] and Srivastava [20,56], it is attractive to envisage that the γ-hydride formation in the α-phase occur through an intermediate β step. It is possible that as hydrogen segregation occurs in certain localized regions within the α phase, these microscopic regions first transform into the β structure which finally goes over to the γ-hydride structure to accommodate the large concentration of hydrogen atoms. Since direct experimental evidences in support of this step wise transformation, $\alpha \rightarrow \beta \rightarrow \gamma$, have not been obtained, the size of the embryonic β-phase appearing in the path of the $\alpha \rightarrow \gamma$ transformation can not be ascertained.

4.2. Active eutectoid decomposition in Zr-based alloys

Active eutectoid systems [57] are those in which the β-phase decomposes into the product phases so fast that it cannot be suppressed even by a rapid quenching. This decomposition is observed in alloys of near-eutectoid compositions. The state of aggregation of the decomposition products in such alloys is lamellar, so that a fine, pearlite like microstructure is obtained on rapid cooling. Systematic study on alloy systems exhibiting active eutectoid decompositions have revealed [7] that active eutectoid decomposition occurs in those where (i) the eutectoid temperature is high, (ii) the eutectoid composition is solute-lean and (iii) the intermetallic phase resulting from the reaction is rich in the base metal. The microstructural observations made on a β-quenched, near-eutectoid (Zr–1.6 wt% Cu; $\beta \rightarrow \alpha + Zr_2Cu$) alloy, which represent a typical case of active eutectoid, could be summarized as follows:

(i) The quenched material consists of several colonies with lamellar structure, consecutive lamellae of the α-phase

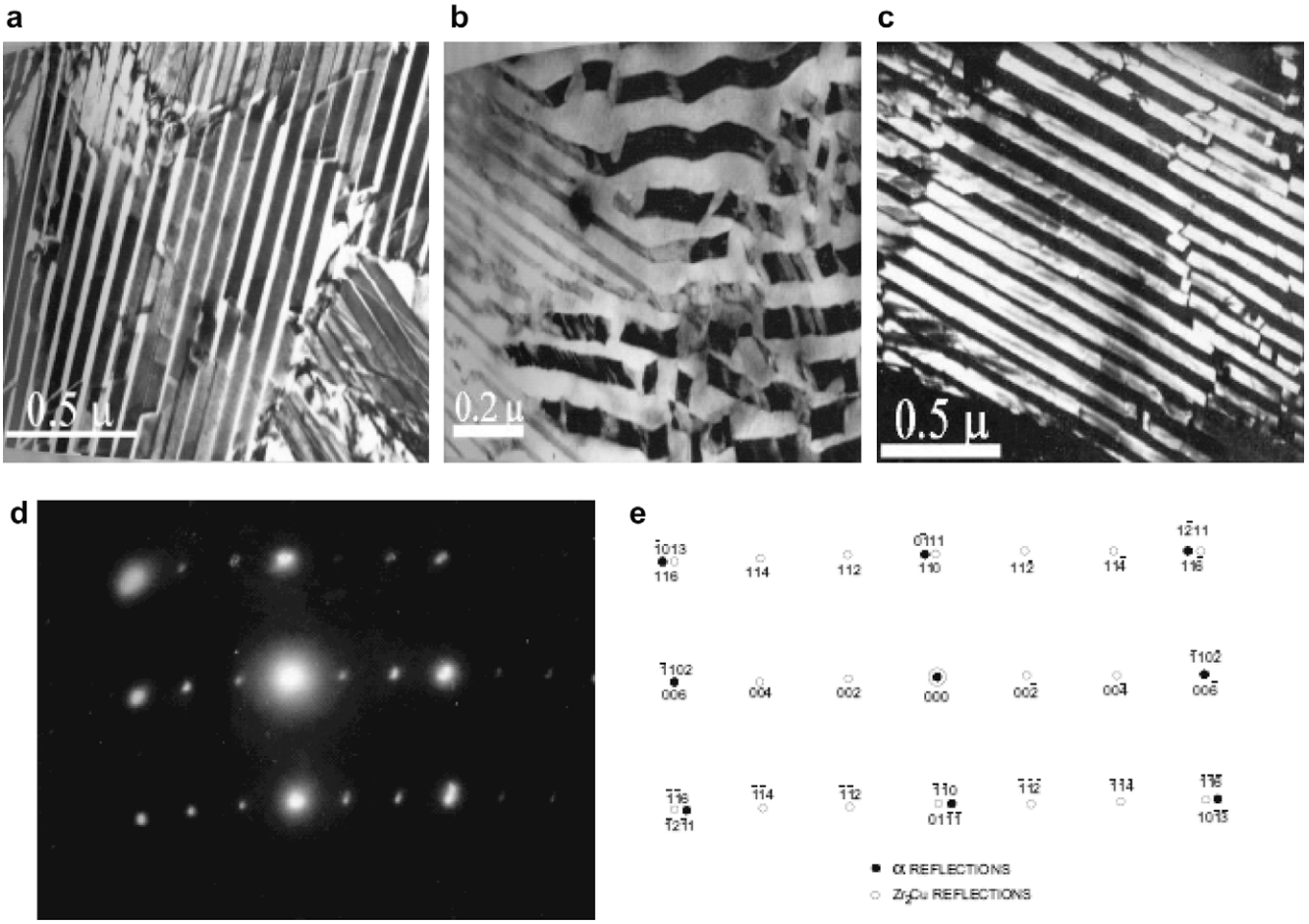

Fig. 17. Microstructure of active eutectoid product in Zr–1.6 wt% Cu (a) period and straight lamellae of α + β′ structure resembling internally twinned martensite structure. (b) Straight lamellae degenerating into wavy lamellae. (c) Dark (β′ reflection) field image of α + β′ structure. (d) Composite SAD pattern showing orientation relationship between α and β′ phase and (e) key to the pattern.

being separated by ribbon like features. In a given cell, the α-lamellae have a single crystallographic orientation and so have the ribbons.

(ii) There are broadly two types of morphologies observed; one with straight lamellar and other with wavy and broken lamellas (Fig. 17(a)–(c)). In the transition region, a one to one correspondence between the straight and the wavy segments exists.

(iii) The average colony size and the average interlamellar spacing are about 2.0 and 0.1 μm, respectively.

Based on evidences provided by selected area diffraction and also by elemental analysis of the phases it was inferred that the ribbons comprised of a phase similar but not identical to Zr_2Cu (Fig. 17(d)–(e)). The matching was better in regions with wavy ribbons than in regions with straight ribbons. Assuming the phase

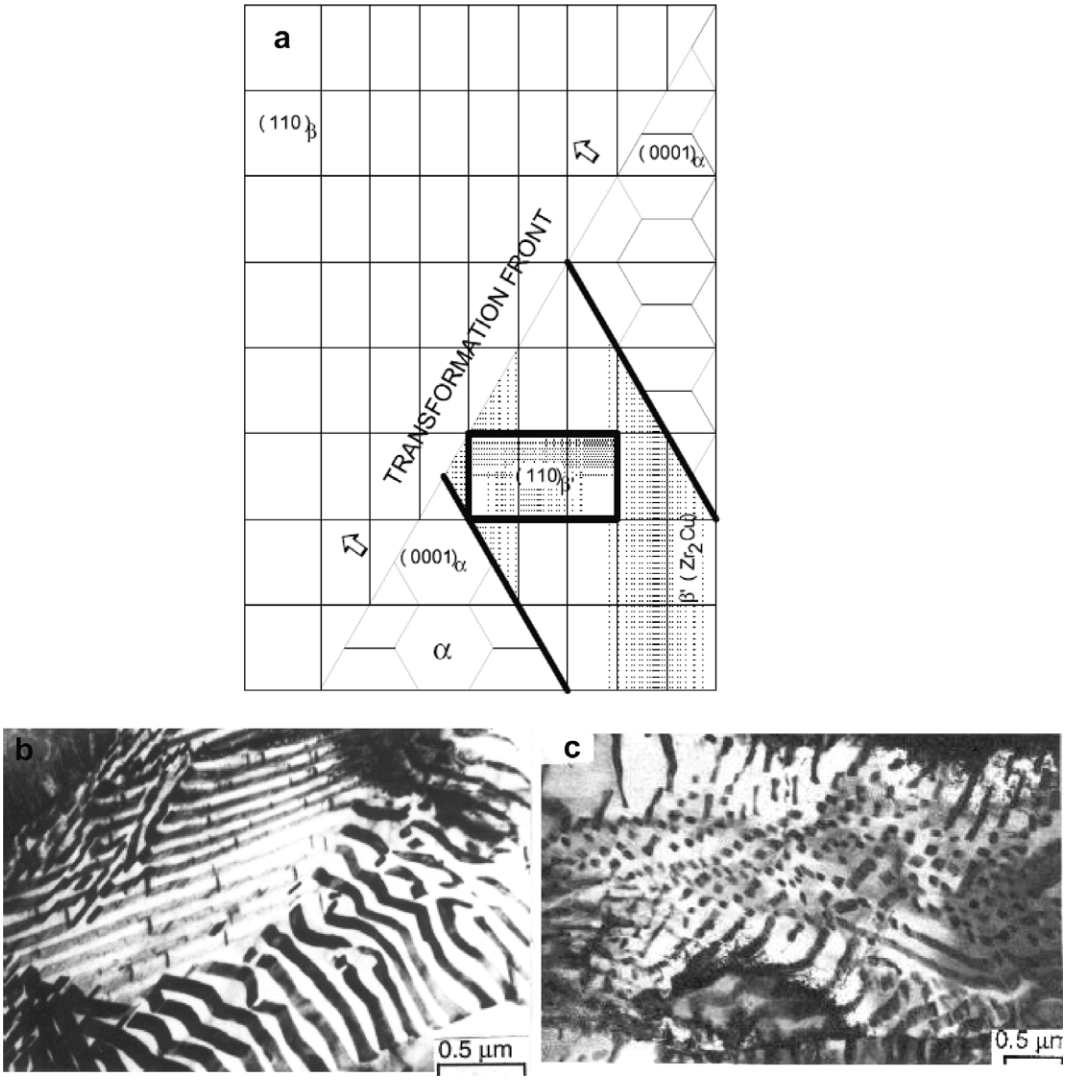

Fig. 18. (a) Schematic presentation of the lattice correspondences between the parent β-phase and the product α and Zr_2Cu based phase. (b) and (c) Microstructures of active eutectoid product in Zr–3 wt% Fe.

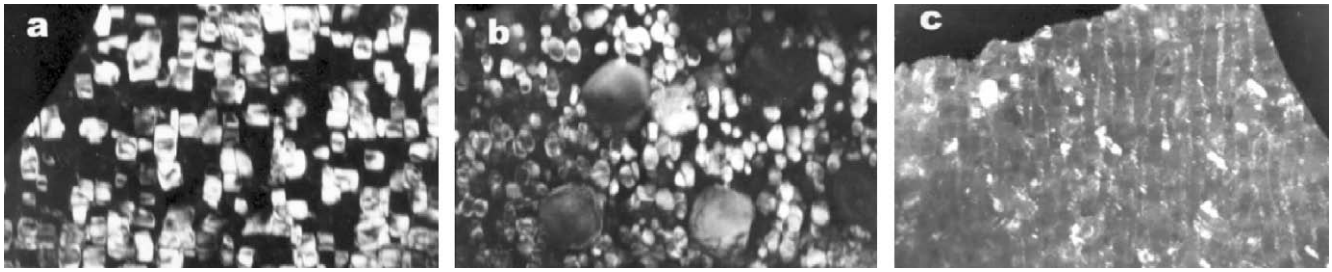

Fig. 19. As-rapidly-solidified microstructures of Zr–Al based alloys where cuboids of the ordered ω-phases could be seen aligned along the ⟨100⟩ direction which is also the direction of spinodal decomposition.

constituting the ribbons to be the Zr_2Cu phase, the following orientation relationship between the two phases could be expressed as:

$$(0001)_\alpha // (013)_{Zr_2Cu}; \quad [\bar{1}100]_\alpha // [0\bar{3}1]_{Zr_2Cu}$$

This orientation relationship (Fig. 17 (d)) is consistent with that observed between the α – and the Ti_2Cu phases in the Ti–Cu system [58] which also exhibit active eutectoid decomposition.

In the case of Zr–Cu alloys it was possible to show that the Zr_2Cu phase can be derived by stacking three bcc cells and by introducing ordering in it [7]. Using such relationships and the observed orientation relationship between the α and the Zr_2Cu phases, the orientation relation between the parent β-and the α-phases has been found to match with the Burgers relation. Using SAD pattern analysis it is also possible to show that the metastable phase constituting the ribbons has attained a certain extent of long range order and this has resulted in an approximately three fold increase in the dimension of the bcc unit cell in the [001] direction. Based on these observations it has been suggested that during β-quenching, the β-phase decomposes into a mixture of the α-phase and a partially ordered phase. Regions containing straight and wavy lamellae in the same colony possibly correspond to different levels of Cu enrichment, and therefore, to different degrees of long range order in the ordered β-phase. The crystallographic description of the lamellar product structure with respect to the parent β-structure is illustrated schematically in Fig. 18. As suggested in figure presence of a lattice correspondence between the two product phases decomposing from the β-phase essentially require cooperative atom movements and presence of partial order within the second phase necessitates diffusion of copper atoms.

As Burger relationship was maintained between β and the α phases, the interfaces between these phases would be expected to be coherent and glissile. The boundaries separating the β-phase and the second phase lamellae would also be expected to be glissile in view of the one to one lattice correspondence exists between the two. However, redistribution of copper atoms ahead of advancing front is a prerequisite step which would cause 15% contraction in the bcc unit cell and also introduce long range ordering. In view of the fact that solubility of Cu in α-Zr is much smaller than that in β-Zr and anomalous diffusion possible in β-Zr, continuous flow of Cu atoms ahead of the advancing transformation front is possible. A simplified analysis has been carried out with a view to compare the observed reaction rates with those estimated. It has been found that the observed and the estimated growth rates are more or less of the same order at temperatures not far below the eutectoid tem-

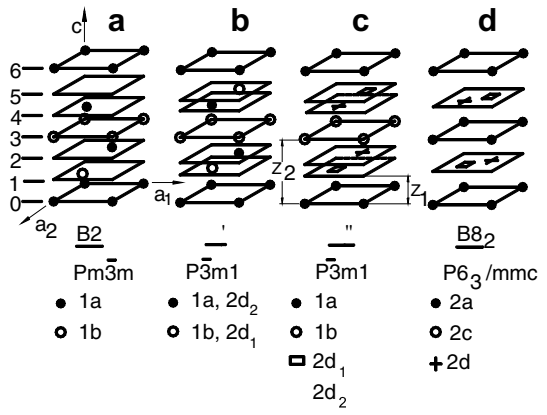

Fig. 20. The lattice correspondence between ordered derivatives of bcc (B2) and the ordered omega structures. Different atomic sites and arrangements of the $(222)_{bcc}$ planes is shown. Gradual and complete collapse of the two pairs of the (222) planes and chemical ordering leading to changes in structural symmetry are shown. Symmetry analysis is shown in Fig. 23.

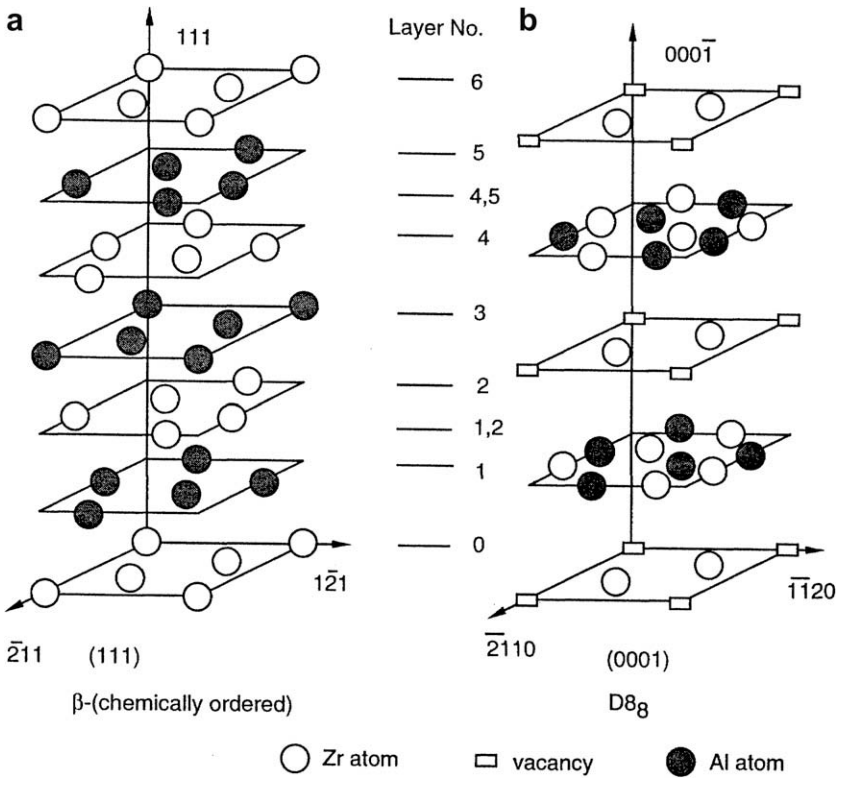

Fig. 21. Lattice correspondence between the ordered bcc (B2) and the $D8_8$ structures. The collapse of {222} planes of the bcc structure (designated as 1 and 2 or 4 and 5) at the intermediate positions (designated as 1, 2 or 4, 5) would produce the $D8_8$ structure. (a) The atomic arrangement in the B2 unit cell. (b) The atomic arrangement in the $D8_8$ unit cell.

perature. This analysis emphasizes the fact that solute partitioning between the two product phases would be quite significant in spite of the extremely fast reaction rates. This is possible due to rapid anomalous diffusion in the β-phase and the exceedingly small interlamellar spacing in the decomposition product.

In the case of Zr_3Fe, however, such a simple structural relationship is not apparent. Nevertheless, from considerations of reaction kinetics and post-reaction microstructure, the decomposition process does appear to be very similar in this case too.

In short, in active eutectoid decomposition, role of underlying lattice correspondence plays an important role. This helps in the formation of the glissile interfaces and also in maintaining lattice registry during phase transformation.

4.3. Formation of ordered derivatives of the ω-phase

The formation of ordered omega structures can be viewed as a superimposition of composition and displacement modulations. The transformation from β to the ordered omega structures has been encountered in Zr–Al based systems. Banerjee et al. [59] have reported the occurrence of the $\beta \rightarrow B8_2$ in the rapidly solidified Zr–27 at.% Al alloy which underwent prior spinodal decomposition. Fig. 19 shows the as-rapidly-solidified microstructures of Zr–Al based alloys where cuboids of the ordered ω-phases are seen aligned along the ⟨1 0 0⟩ direction. Spinodal decomposition in these alloy resulted in the formation of Al rich nodes at the junction of the ⟨1 0 0⟩ modulations, which subsequently transformed into a single Zr_2Al particle suggesting a homogeneous transformation where formation of the particle has not experienced any nucleation barrier. The matching of the size of the particle with the spinodal wave length, which is 20 nm, could be taken as evidence for the above argument.

The ordered ω-phase transformation in this case appears to involve the following steps in the overall transformation:

(i) Congruent solidification of the liquid phase into the supersaturated β-phase.
(ii) Development of the concentration fluctuation in the supersaturated β-phase.
(iii) Formation of the ordered ω-phases in the solute-rich regions.
(iv) Transformation of the metastable phases into the relatively stable phases.

It has been shown that the $\beta \rightarrow B8_2$ structural transition would require a combination of the collapse of the layers (1, 2; 4, 5; etc.) and a chemical ordering (Fig. 20). The fact that such a lattice correspondence indeed exists in several real systems has been demonstrated [41,59,60]. Based on this correspondence the lattice parameters, a and c, of the $B8_2$ phase can be expressed in terms of the lattice parameter, a_β

$$a_B = \sqrt{2}a_\beta; \quad c_B = 6\ d_{222} = \sqrt{3}a_\beta$$

where B stands for the $B8_2$ structure. Substituting the extrapolated values of a_β for Zr–33 at.% Al the lattice parameters of Zr_2Al work out to be the following:

$$\text{For } Zr_2Al: a = 0.4852 \text{ nm} \quad c = 0.5942 \text{ nm}$$

Tewari et al. [61] have observed the presence of yet another ordered ω structure which has the $D8_8$ structure (prototype Mn_5Si_3). This structure with a hexagonal unit cell possesses 18 Wyckoff positions. The stacking sequence and the lattice correspondence in the $D8_8$ structure are compared with those in the B2 structure in Fig. 21. This Figure also depicts the lattice correspondence between these two structures. Based on this correspondence the lattice parameters of the $D8_8$ phase are related to that of the ordered β-phase (B2 structure) as

$$a_{D8_8} = \sqrt{6}a_\beta \quad \text{and} \quad c_{D8_8} = 6d_{222,\beta} = \sqrt{3}a_\beta$$

In the case of Zr_5Al_3, the substitution of the corresponding a_β (=0.3455 nm) value yields the a and c parameters of the $D8_8$ phase as 0.8464 nm and 0.5984 nm, respectively, which are fairly close to the experimentally obtained lattice parameters (a = 0.845 nm and c = 0.5902 nm) of the equilibrium Zr_5Al_3 phase. Fig. 21 shows that the $D8_8$ structure also can be generated from the B2 structure by a combination of lattice collapse and chemical ordering. The pairs of {2 2 2} planes which collapse in the $B8_2$ and in the $D8_8$ structure are essentially the same. In case of the $D8_8$ structure an ordered array of vacancies is necessary in those B2 planes which remain

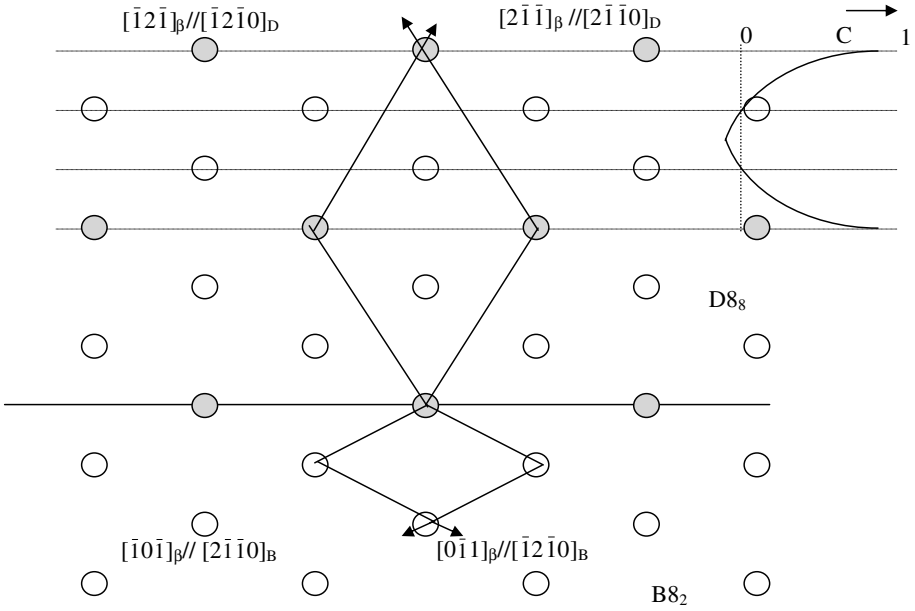

Fig. 22. Schematic of the atomic arrangement on the basal planes of the $B8_2$ and the $D8_8$ structures. As may be noticed the two structures differ due to the occupancy of the sites indicated by vacancies.

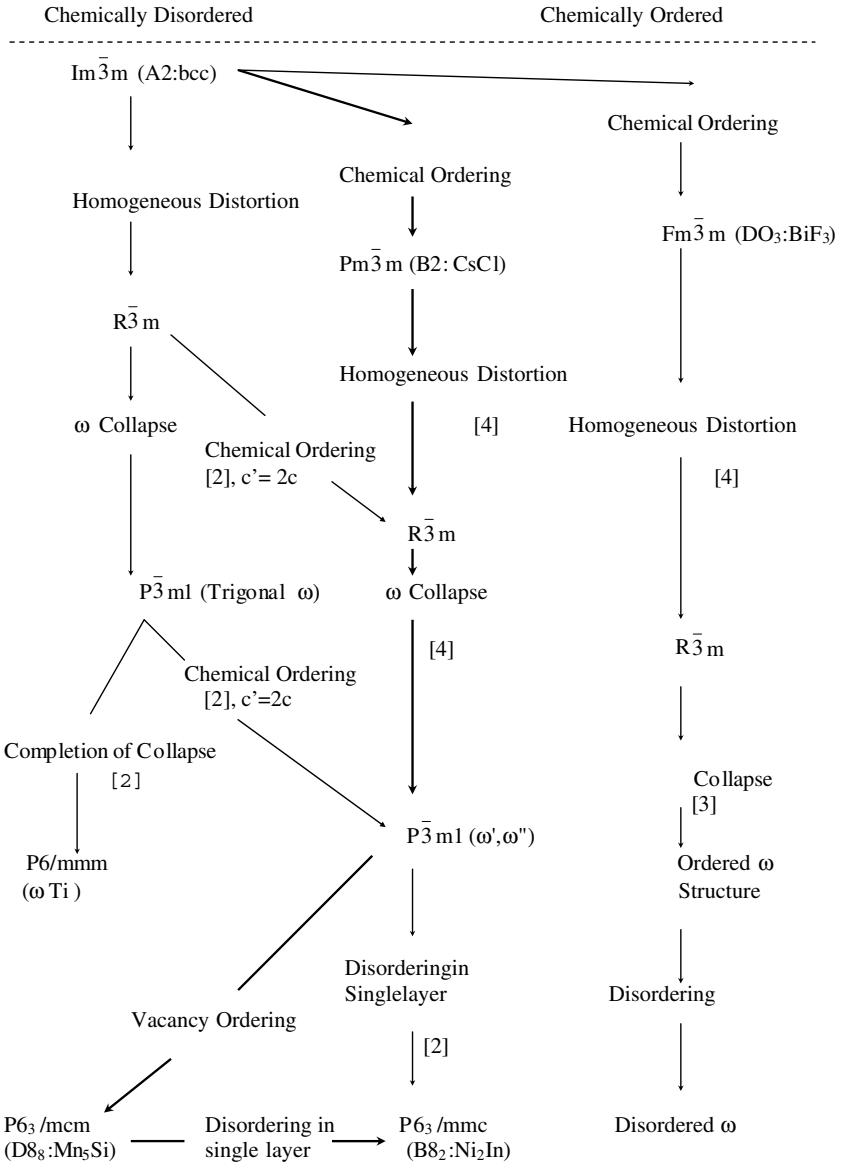

Fig. 23. Symmetry tree representation of phase transformations of β → ω related phase. The bold lines represent the sequence of phase transformations observed in the present study whereas the other sequences of phase transformations are reported in the literature.

undisplaced during the collapse. This is essential for meeting the stoichiometric requirement. The difference between the $B8_2$ and the $D8_8$ structures lies in whether the 2(b) positions are occupied by Zr atoms or (are) vacant (Fig. 22). The fact that 2 vacancies for 18 atom positions per unit cell are required for the formation of the $D8_8$ structure necessitates the retention of a high concentration of vacancies in the parent B2 structure and an ordered arrangement of these vacancies. If the 2(b) positions are occupied with Al atoms, a stoichiometry of Zr_5Al_4, having a Ga_4Ti_5 structure, is attained.

Bendersky et al. [60] have constructed the symmetry tree showing symmetry changes that occur during partial and complete lattice collapse associated with the β → ω displacement ordering and accompanying chemical ordering by coupled displacive–replacive ordering processes (Fig. 23).

5. Concluding remarks

Pure Zr and its alloys show variety of phase transformation – both diffusionless as well as diffusional. In many of these transformations the role of the Burgers lattice correspondences between the parent β and the product α phases is important. Interfaces between the product phases as well as between the parent and the product phase provide clues for the mechanisms of the phase transformation. In case of martensitic transformation, using phenomenological theory of martensite it was possible to predict the habit plane, morphology and nature of the defects presents in the product phase. In a similar way in diffusional transformations role of the invariant line strain in predicting the direction of the rapid growth is vital.

In many transformations, underlying lattice correspondence between the product and parent phase determines the kinetics, morphology and orientation relationship between the phases during phase transformation in many Zr base alloys, in particularly, in alloy systems where one of the precipitating phase is an intermetallic system.

Understanding these phase transformation has helped in understanding the evolution of the microstructures under different conditions which, in turn, helped in optimizing the fabrication routes as well as in understanding the performance of zirconium in presence of impurities like hydrogen.

In short, studies on the evolution of microstructures in zirconium based alloys have fundamental importance as well as practical implications. A detail description of these transformations can be obtained in a recent publication [62].

References

[1] D.L. Douglass, The Metallurgy of Zirconium, Internal Atomic Energy Agency, Vienna, 1971.
[2] G.L. Millar, Zirconium, Butterworth Scientific Publications, London, 1957.
[3] D. Srivastava, G.K. Dey, S. Banerjee, Metal. Mater. Trans. A 26A (1995) 2707.
[4] G.J.C. Carpenter, Can. Metall. Quart. 24 (1985) 251.
[5] R.F. Heheman, Can. Metall. Quart. 11 (1972) 201.
[6] E.S.K. Menon, S. Banerjee, R. Krishnan, Metall. Trans. 9A (1978) 1213.
[7] P. Mukhopadhyay, E.S.K. Menon, S. Banerjee, R. Krishnan, Metall. Trans. 10A (1979).
[8] Lalit Kumar, R.V. Ramanujan, R. Tewari, P. Muhopadhyay, S. Banerjee, Scripta Mater. 40 (1999) 723.
[9] C.E. Coleman, D. Hardie, J. Less Common Met. 11 (1966) 168.
[10] M. Kiran Kumar, I. Samajdar, N. Venkatramani, G.K. Dey, R. Tewari, D. Srivastava, S. Banerjee, Acta Mater. 51 (2003) 625.
[11] B.A. Chedale, S.A. Aldrige, C. EElls, Can. Metall. Quart. 11 (1972) 121.
[12] A.M. Garde, H.M. Chung, T.F. Kassner, Acta Metall. 26 (1978) 153.
[13] G. Ostberg, R. Attermo, J. Nucl. Mater. 5 (1962) 120.
[14] T. Konishi, K. Matsuda, H. Teranishi, Can. Metall. Quart. 11 (1972) 165.
[15] J.K. Chakravartty, S. Banerjee, Y.V.R.K. Prasad, M.K. Asundi, J. Nucl. Mater. 187 (1992) 260.
[16] S.K. Sikka, Y.K. Vohra, R. Chidambaram, Prog. Mater. Sci. 27 (1982) 245.
[17] J.C. Jamison, in: K.A. Gschneidner Jr., M.T. Hepworth, N.A.D. Parlee (Eds.), Metallurgy at High Pressures and Temperature, Gorden and Breach, New York, 1964, p. 201.
[18] G.K. Dey, R. Tewari, S. Banerjee, G. Jyoti, S.C. Gupta, K.D. Joshi, S.K. Sikka, Acta Mater. 52 (2004) 5243.
[19] G. Jyoti, K.D. Joshi, S.C. Gupta, S.K. Sikka, G.K. Dey, S. Banerjee, Philos. Mag. Lett. 75 (1997) 291.
[20] D. Srivastava, Beta Phase Transformation in Zirconium Based Alloys, PhD thesis, Indian Institute of Sciences, 1996.
[21] S. Banerjee, R. Krishnan, Acta Metall. 19 (1971) 1317.
[22] S. Banerjee, R. Krishnan, Metall. Trans. 4 (1973) 1811.
[23] P. Grant, J.W. Christian, Acta Metall. 14 (1959) 529.
[24] D.S. Lieberman, T.A. Read, M.S. Wechsler, J. Appl. Phys. 28 (1957) 532.
[25] J.K. Mackenzie, J.S. Bowles, Acta Metall. 5 (1957) 137.
[26] Yu.A. Bagaryatskiy, G.I. Nosova, Fiz. Met. Metalloved 13 (1962) 415.
[27] J.C. Williams, D. deFontaine, N.E. Paton, Metall. Trans. 4 (1973) 2701.
[28] S. Banerjee, R. Tewari, G.K. Dey, Int. J. Mater. Res. 97–7 (2006) 963.
[29] C.P. Luo, G.C. Weatherly, Metall. Trans. 19A (1988) 1153.
[30] E.S.K. Menon, S. Banerjee, R. Krishnan, Metall. Trans. 9A (1978) 1213.
[31] S. Banerjee, S.J. Vijaykar, R. Krishnan, J. Nucl. Mater. 62 (1976) 229.
[32] K. Muraleedharan, D. Banerjee, S. Banerjee, S. Lele, Philos. Mag. A 71 (1995) 1011.
[33] U. Dahmen, Acta Metall. 30 (1982) 63;
U. Dahmen, P. Feranson, K.H. Westmacott, Acta Metall. 32 (1984) 803.
[34] U. Dahmen, K.H. Westmacott, Acta Metall. 34 (1986) 475.
[35] V. Perovic, G.C. Weatherly, Acta Metall. 37 (1989) 813.
[36] S. Banerjee, G.K. Dey, D. Srivastava, S. Ranganathan, Metall. Trans. 28A (1997) 2201.
[37] J.M. Howe, T. Abinandan, C.S. Chiang, T. Furuhara, N. Prabhu, H.I. Aaronson, Scripta Metall. 21 (1987) 1639.
[38] T. Furuhara, T. Ogawa, T. Maki, Philos. Mag. 72 (1995) 175.
[39] T. Furuhara, K. Wada, T. Maki, Metall. Trans. A 26 (1995) 1971.
[40] K.A. Bywater, J.W. Christian, Philos. Mag. 25 (1972) 1275.
[41] R.F. Hehemann in: Proceedings of USAEC Symposium on Zirconium Alloy Department, GEAP-4089, L10, 1962.
[42] S. Banerjee, R.W. Cahn, Acta Metall. 31 (1983) 721.
[43] H.J. McQueen, D.L. Bourell, J. Mater. Shaping Technol. 5 (1988) 163.
[44] I. Weiss, S.L. Semiatin, Mater. Sci. Eng. A 236 (1999) 243.
[45] M.J. Lutton, J.J. Jonas, Can. Metall. Quart. 11 (1972) 79.
[46] D.J. Abson, J.J. Jonas, J. Nucl. Mater. 42 (1973) 73.
[47] J.K. Chakravartty, Y.V.R.K. Prasad, M.K. Asundi, Metall. Trans. 22A (1991) 829.
[48] J.K. Chakravartty, Optimization of hot workability and control of microstructure in zirconium and zirconium alloys using processing maps, PhD (Engg.) thesis, Indian Institute of Science, Bangalore, India, 1992.
[49] J.K. Chakravartty, S. Banerjee, Y.V.R.K. Prasad, Scripta Metall. 26 (1992) 75.
[50] J.K. Chakravartty, Y.V.R.K. Prasad, M.K. Asundi, in: Ninth International Symposium, ASTM, Philadelphia, vol. 44, ASTM STP, 1992, p. 1132.
[51] S.S. Sidhu, L.R. Heaton, F.P. Campos, D.D. Zauberis, Am. Chem. Soc. (1963).
[52] G.K. Dey, S. Banerjee, P. Mukhopadhyay, J. Phys. C 4 (1984) 327.
[53] G.K. Dey, S. Banerjee, J. Nucl. Mater. 124 (1984) 219.
[54] P.E. Flewitt, P.J. Ash, A.G. Crocker, Acta Metall. 24 (1976) 669.
[55] G.C. Weatherly, Acta Metall. 29 (1981) 501.
[56] D. Srivastava, S. Neogy, G.K. Dey, S. Banerjee, S. Ranganathan, Mater. Sci. Eng. A 397 (2006) 138.
[57] R.I. Jafee, Prog. Met. Phys. 7 (1958) 69.
[58] J.C. Williams, in: R.I. Jafee, H.M. Burte (Eds.), Phase Transformation in Ti alloys: A Review Titanium Science Technology, vol. 3, Plenum, 1973, p. 1433.
[59] S. Banerjee, R. Tewari, P. Mukhopadhyay, Prog. Mater. Sci. 42 (1997) 109.
[60] L.A. Bendersky, W.J. Boettinger, B. Burton, F.S. Biancaniello, C.B. Shoemaker, Acta Metall. 38 (1990) 931.
[61] R. Tewari, P. Mukhopdyay, S. Banerjee, L.A. Bendersky, Acta Mater. 24 (1999) 1307.
[62] S. Banerjee, P. Mukhopadyay, Phase Transformation in Alloys Examples from Titanium and Zirconium, Pergamon, UK, 2007.